Project co-funded by EC. Grant no 260105.

D3.1.3 Annex 2

Equipment list and summary sheets
Technical layout and evaluation of CPOx reformer

Numerical simulations (IST)

Issue Date	30 September 2011 (M12)
Deliverable Number	D3.1.3
WP Number	WP3: Building and district tailoring of SOFC
Status	~~Started / Draft / Consolidated / Review / Approved /~~ Submitted ~~/ Accepted by the EC / Rework~~
Author(s)	S. Fernandes, J. Navalho (IST)

Dissemination level		
PU	Public	
PP	Restricted to other programme participants (including the Commission Services)	**X**
RE	Restricted to a group specified by the consortium (including the Commission Services)	
CO	Confidential, only for members of the consortium (including the Commission Services)	

Document history

Version	Date	Author	Description
0.1	09/26/11	Sofia Fernandes	CFD analysis report
0.2	09/29/11	J. Navalho	Detailed chemistry report
0.3	09/30/11	J. Chaves Pereira	Review
0.4	09/30/11	J. Carlos Pereira	Review

Disclaimer
The information in this document is provided as is and no guarantee or warranty is given that the information is fit for any particular purpose. The user thereof uses the information at its sole risk and liability.
The document reflects only the author's views and the Community is not liable for any use that may be made of the information contained therein.

Table of contents

Summary

An SOFC-based micro-CHP system is developed within the FC-DISTRICT project. This report deals with the development of the Catalytic Partial Oxidation (CPOX) reactor, which will be used as reformer in the micro-CHP system of FC-DISTRICT. Until now two prototypes of the reformer were designed.
This Annex deals with the CFD tri-dimensional analysis of the two reformer prototypes as well as a pre-heater and a pre-mixer prototype during the first year of the project.

1. Introduction

An SOFC based micro-CHP system is to be built in the framework of the project FC-DISTRICT. A CPOX reactor is utilized to convert a natural gas/air-mixture into a H_2 and CO rich syngas, which is fed to the high temperature SOFC stack.

IST is supporting the development of the CPOX reactor with numerical simulations. Star-CCM+ software was used to carry out simulations of two prototypes of the CPOx reformer as well as related components: the CPOx Pre-heater and CPOx Pre-mixer.

The aim of these simulations is to understand the details of the gas flow and heat transfer (where it applies) inside the components in order to either show the components performance or make improvements. Characteristics such as flow patterns, mixing quality, pressure loss and temperature distribution are evaluated and, when possible, validated against experimental data.

2. First CPOx reactor prototype

2.1 Introduction

The 1st reactor prototype was manufactured by EBZ and was sent to TUBAF for detailed characterization for operation with methane. IST undertook all the numerical simulations to predict pressure losses and flow patterns inside the reformer.

2.2 Geometry

The reactor consists of a conical section, where the premixed fuel/air-mixture enters the reformer, a cylindrical part, where the catalyst is fixed and a conical section at the outlet of the reformer. The following images and table describe the simulated geometry.

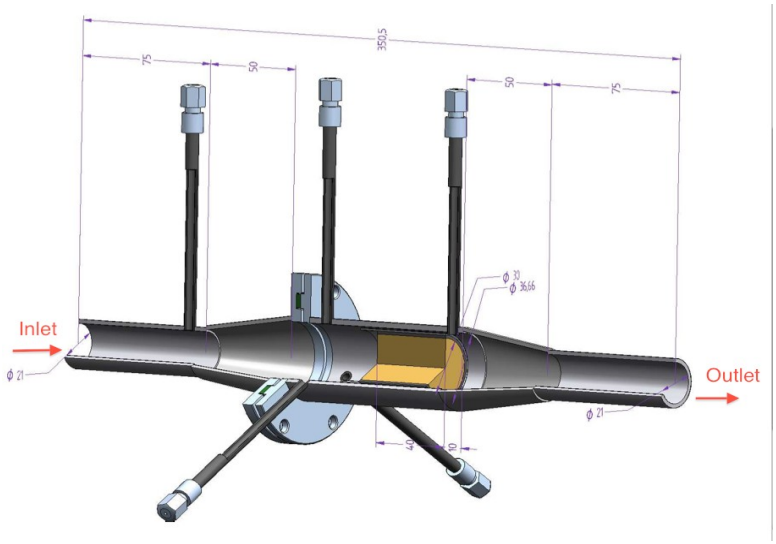

Figure 1: CPOx 1st prototype

For simulation purposes, advantage was taken of the Reformer's radial symmetry. Hence only a 30 deg longitudinal slice of the geometry was modelled, meshed and simulated. Due to the stated symmetry properties of this geometry, the physical phenomena inside the full reformer can be simulated this way without loss of information.

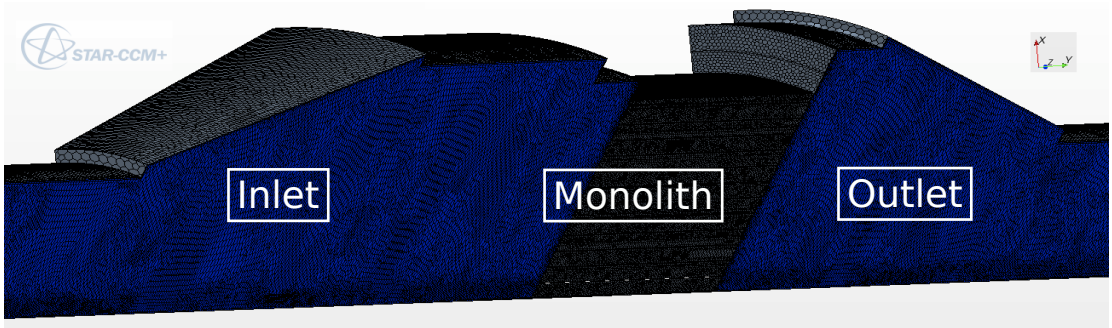

Figure 2: CPOx 1st prototype - simulated geometry

The noble metal based catalyst sits on a 600cpsi ceramic monolith. Its 3D geometry was modelled using Star-CCM+'s CAD program.

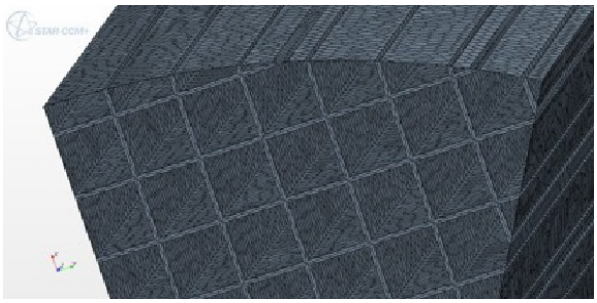

Figure 3: CPOx 1st prototype - monolith

Geometry characteristics			
Global reformer		**Monolith**	
Simulated arc	30 deg	Fabricator	NGK
Total length	200 mm	Cell density	600 cpsi = 0,93 c/mm²
Max. diameter	36 mm	Void fraction	86% (*)
Monolith length	40 mm	Mean pore diameter	0,960 mm
Monolith diameter	30 mm	Wall thickness	0,077 mm
(*) - In the first geometry of the CPOx reformer's simulation the thickness of the monolith's washcoat was not considered.			

Table 1: CPOx 1st prototype - Geometrical characteristics

2.3 Mesh

A polyhedral mesh with prismatic layers on the walls to account for the boundary layers and extrusions both at the inlet and the outlet was used. Special refinement care was taken at the monolith region. The following images show selected plane sections of the geometry highlighting relevant mesh features. The table below shows global measures of the mesh.

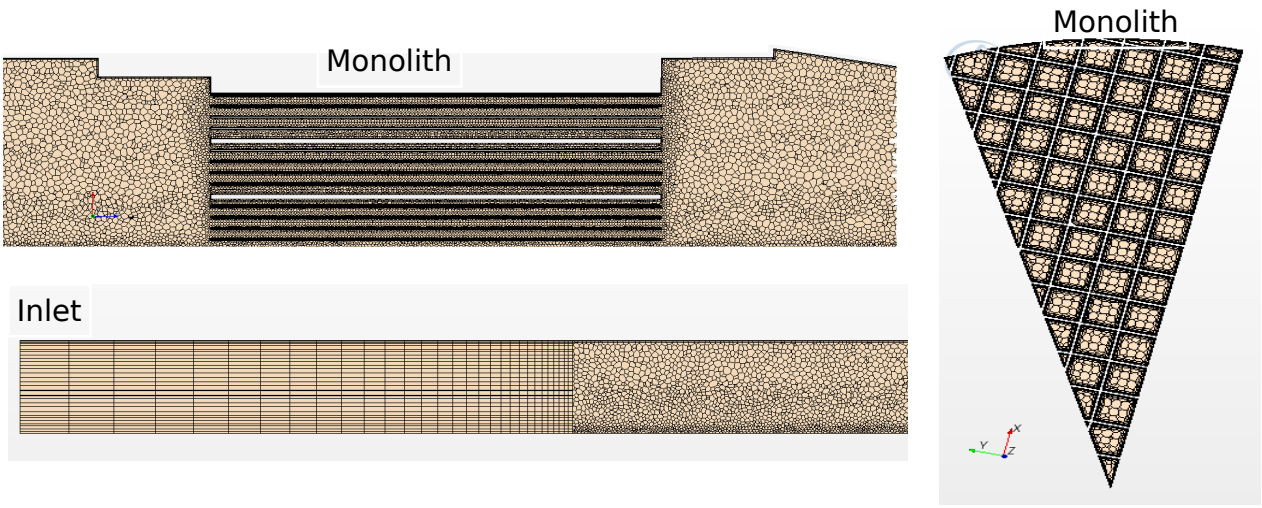

Figure 4: CPOx 1st prototype - Mesh

Overall mesh characteristics	
Total number of cells	1,2 million
Maximum cell base size	0,5 mm
Minimum cell size	0,16 mm

Table 2: CPOx 1st prototype - Mesh characteristics

2.4 Simulation Conditions

2.4.1 CPOx Reformer working condition

According to the experimental data from TUBAF, a selected working point was numerically simulated. The following table summarizes the simulated working point, that corresponds to the micro-CHP working with a power of 1,5kW and with 70% fuel utilization by the fuel cell.

Simulated working conditions	
Inlet temperature	322 ºC
Total mass flow (360deg)	0,557 g/s
Inlet chemical composition	Air (N2, O2) + Methane; lambda = 0,31
Outlet chemical components	CH4, N2, H2, H2O, CO2, CO
Perfectly mixed gas at inlet	

Table 3: CPOx 1st prototype – Working conditions

2.4.2 Numerical models

The simulations were run using the models stated in the following table.

Numerical models	
Time	Steady
Turbulence	K-omega SST
Energy	Isothermal
Density	User-defined (*)
Viscosity	User-defined (*)
Solid (monolith, insulation and steel-tube)	Not included in simulation
(*) - Temperature and chemical composition are simulated indirectly by defining the fluid's density and viscosity.	

Table 4: CPOx 1st prototype – Numerical models

2.4.3 Assumed fields

Since combustion was not be modelled in the 3D simulation, typical temperature and chemical composition profiles were assumed according to the usual values for a catalyst reformer under similar conditions.
The following plots show the simplified temperature and composition profiles assumed in the 3D simulation. The original profiles were obtained in the detailed 1D chemistry simulation developed by Jorge Navalho [1].

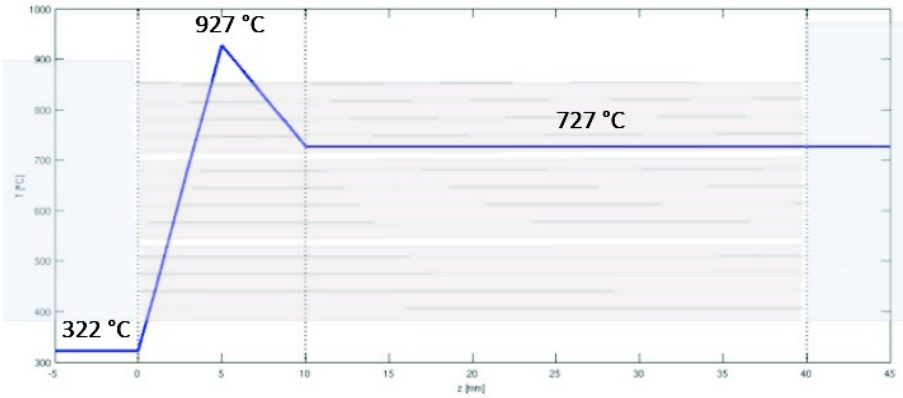

Figure 5: CPOx 1st prototype – Assumed temperature

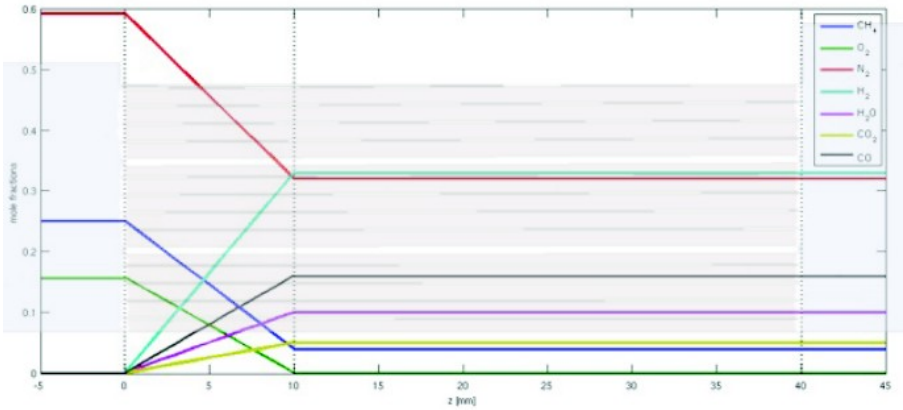

Figure 6: CPOx 1st prototype – Assumed composition

2.4.4 Imposed fields

Density and dynamic viscosity were computed according to the profiles for temperature and chemical composition shown above.
They were imposed in the simulation in order to reflect the effects of temperature and chemical composition variation in the fluid flow.

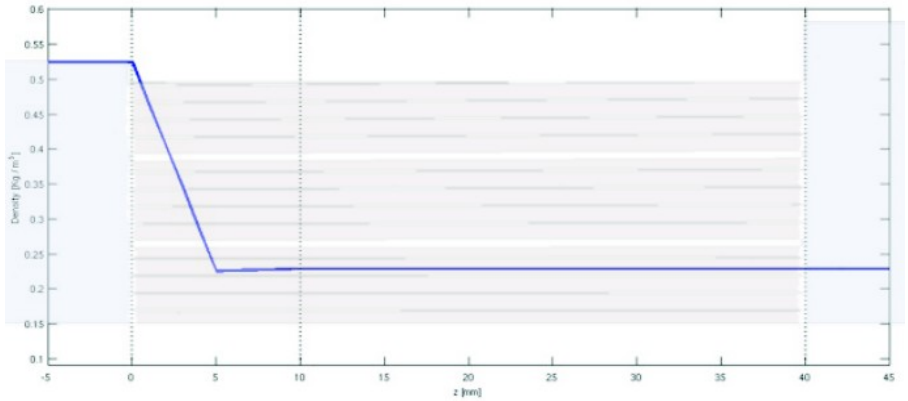

Figure 7: CPOx 1st prototype – Imposed density

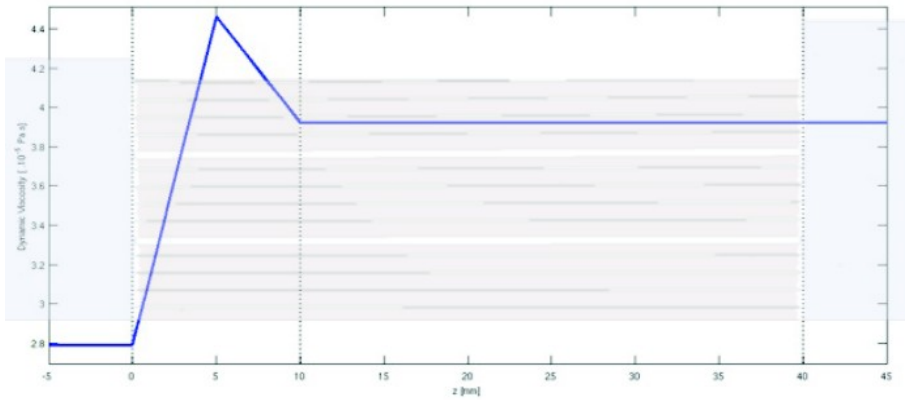

Figure 8: CPOx 1st prototype – Imposed viscosity

2.5 Results

2.5.1 Velocity field

The following images show a longitudinal plane section of the gas velocity inside the CPOx reformer as well as selected detail zones showing relevant features, such as the recirculation bubble at the exit chamber and the velocity profile inside a monolith tube.

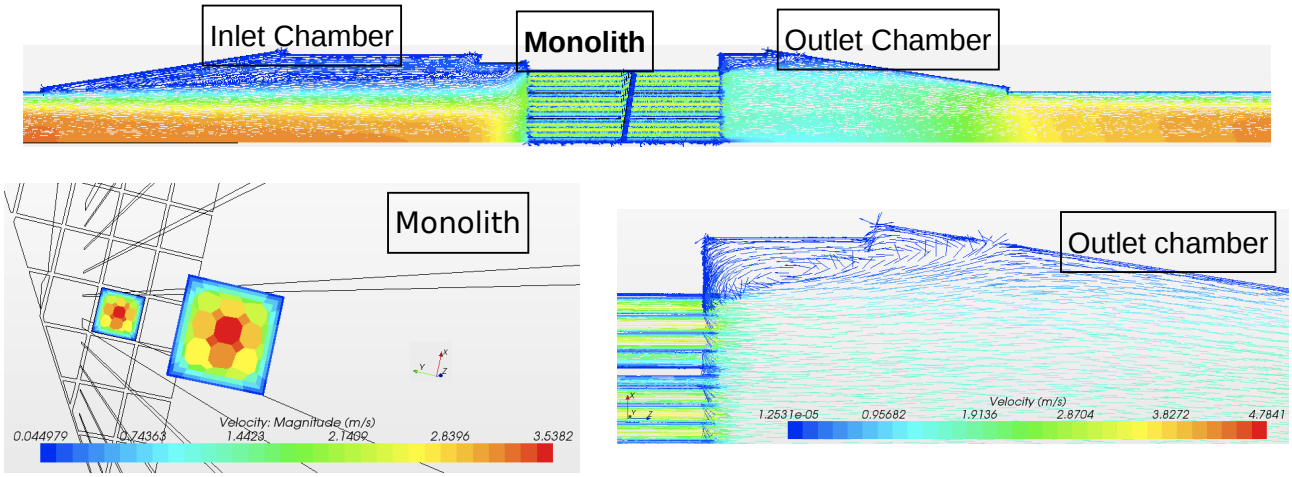

Figure 9: CPOx 1st prototype – Velocity field

A separation zone can be seen in the inlet chamber, which will be analysed in detail in the following sub-section (Streamlines).

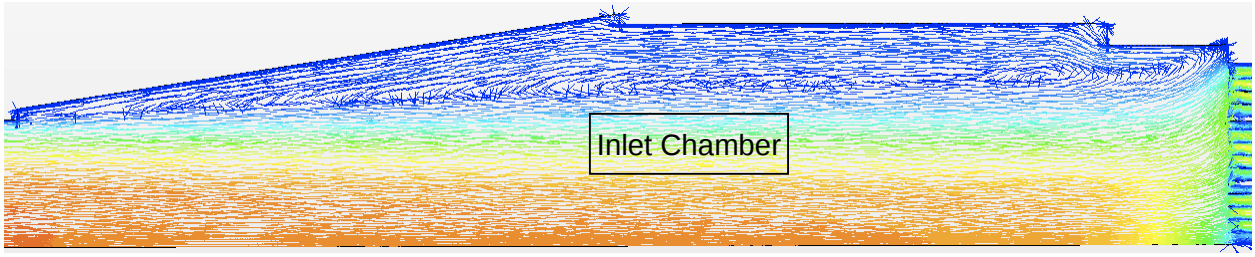

Figure 10: CPOx 1st prototype – Velocity in the inlet chamber

The table below summarizes the velocity field's key values.

Velocities	
Average inlet velocity	1,87 m/s
High speed stream average velocity	1,40 m/s
Average velocity inside monolith	2,09 m/s
Average outlet velocity	4,52 m/s

Table 5: CPOx 1st prototype – Velocities

2.5.2 Streamlines

A tri-dimensional streamline analysis of the flow, based on its velocity field, was conducted. As expected from inspection of the velocity field plots, two main recirculation zones with separated flow can be identified.

The most important one occurs in the first chamber. It's most important effect is on particle residence time, as will be shown below. Regarding the mainstream flow, the recirculation bubble acts like a wall, creating two distinct regions within the inlet chamber: the flow inside the bubble and the mainstream flow.

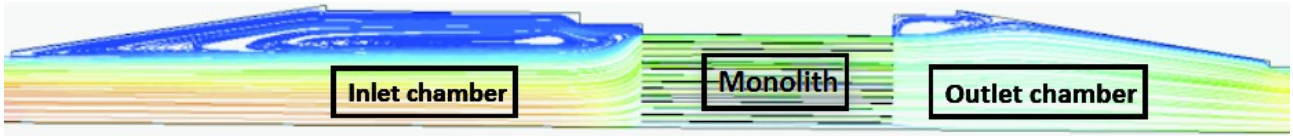

Figure 11: CPOx 1st prototype – Streamlines

Studies show that separation of confined flow is directly related with the divergence angle and local Reynolds number. Both were analysed, leading to the conclusions that this is a laminar flow regime case – in particular for this case Reynolds < 2000. For these conditions a divergence angle smaller than 5deg should avoid flow separation.

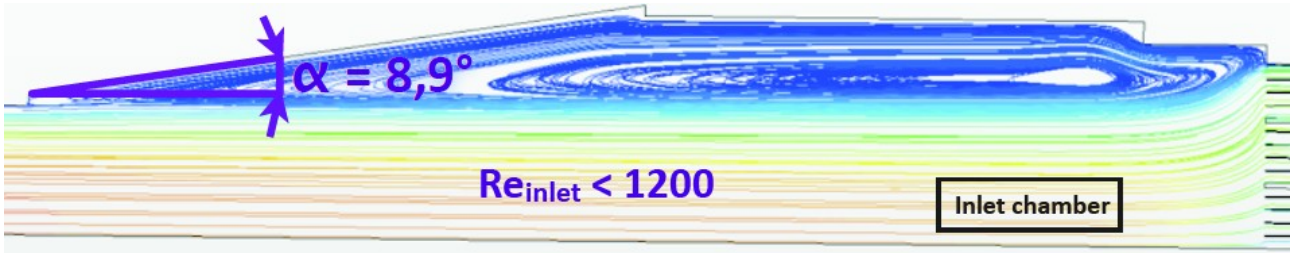

Figure 12: CPOx 1st prototype – Separated flow

The following table briefly states t the relevant reference literature data on this subject.

Tapper angle	Flow separation
Alfa = 5 deg	Reynolds < 2000
Alfa = 10 deg	Reynolds < 4000
Reference: E. M. Sparrow et. al., “Flow separation in a diverging conical duct: Effect of Reynolds number and divergence angle”	

Table 6: CPOx 1st prototype – Flow separation

2.5.3 Residence time

The recirculation bubbles significantly increase the residence time of the particles that enter it. Hence, there is a huge difference in residence time between the main stream flow and the recirculation bubble flow, especially in the first chamber.
The following particle residence time plots highlight this difference and the table below summarizes important values.

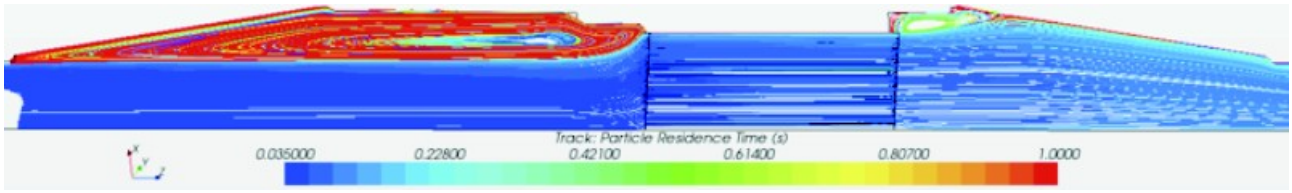

Figure 13: CPOx 1st prototype – Residence time

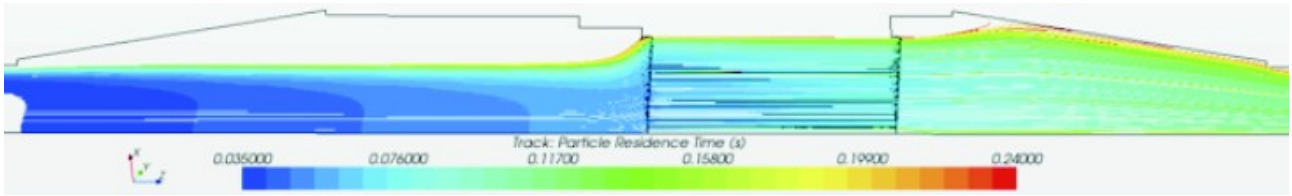

Figure 14: CPOx 1st prototype – Residence time - low

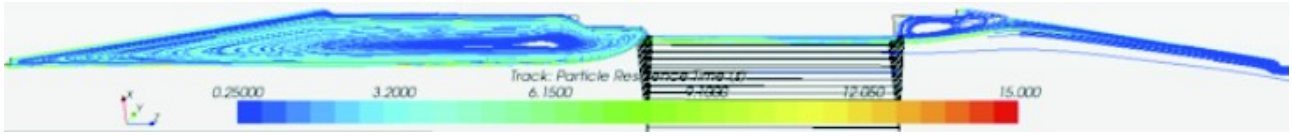

Figure 15: CPOx 1st prototype – Residence time – high

Overall residence time	
Minimum (*)	0,10 s
Average	0,12 s
Maximum (*)	15 s
(*) - These values are estimations based on a random process analysis of particle simulation.	

Table 7: CPOx 1st prototype – Residence time

2.5.4 Pressure

Overall pressure drop is a key design factor, thus a detailed study of pressure profile inside the Reformer was undertaken. The overall predicted pressure drop for the monolith under the simulated working conditions is below 1,1mbar.
It can be seen in the plot below that the main pressure loss occurs inside the monolith region and is proportional to monolith length. The conical outlet adds a small contribution.
The recirculation doesn't affect pressure drop.

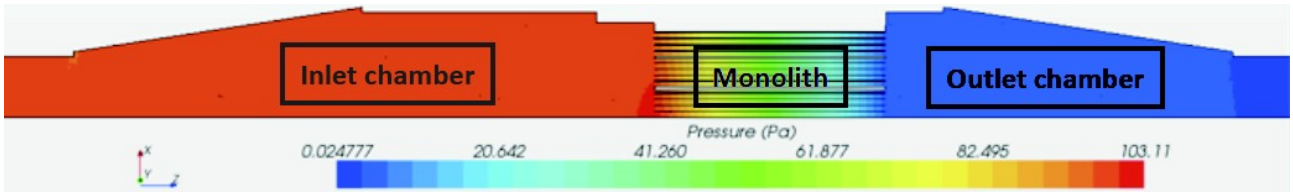

Figure 16: CPOx 1st prototype – Pressure drop

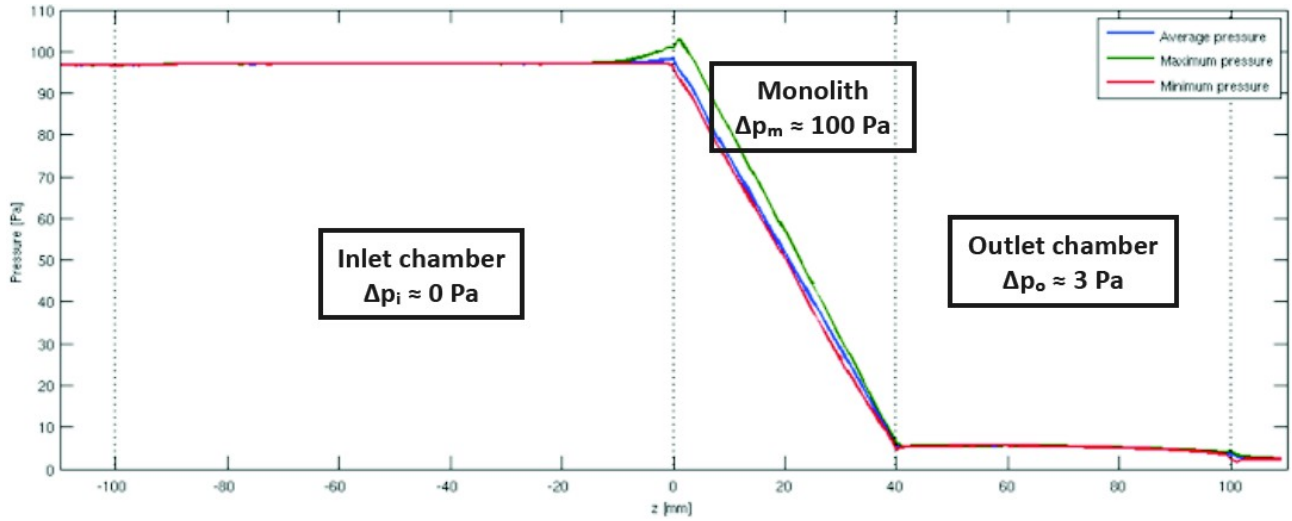

Plot 1: CPOx 1st prototype – Pressure drop

2.6 Conclusions

There's a big recirculation bubble in the inlet chamber conical duct. It acts like a wall on the main flow stream and its main effect is to dramatically increase the residence time of the particles that enter it. A tapper angle smaller than 5deg should make it disappear.

Pressure losses are lower than in previous geometries due to absence of heat shields.

Simulations of later geometries are done under more realistic profiles and considering thermal conduction with the solid.

3. Second CPOx reactor prototype

3.1 Introduction

The second prototype's geometry was simulated for a similar working condition as the first prototype had been. The most important difference is of course the geometry, but also the mesh is more refined in this case and the numerical models are more complete since temperature equation is used for this case. Furthermore, a slice of 45 deg is used for the second prototype instead of the 30 deg used before, in order to improve symmetry qualities.
Objectives are analysis of the flow behaviour inside the CPOx reformer, i.e. pressure loss, flow pattern and residence time.
Combustion is emulated using species molar fraction profiles given by J. Navalho's detailed one-dimensional chemistry simulations.

3.2 Geometry

The CPOx Reformer second prototype is cylindrical shaped with an inlet expansion towards a catalytic coated square monolith. Towards the exit it has a conical compression. For three-dimensional fluid flow simulation purposes the symmetry characteristics of this geometry were taken advantage of to reduce the required computational power. As a result the simulation was run over a longitudinal 45deg slice of the entire geometry. It can be proven that this is equivalent to simulating the entire 360deg geometry.
Regarding the monolith geometry inside, it was designed in CAD software according to NGK's specifications regarding their 600cpsi monolith, which was used in the laboratory prototype.
The following images show the simulated geometry as well as a detail of the monolith geometry contained within.

Figure 17: CPOx 2nd prototype – Simulated geometry

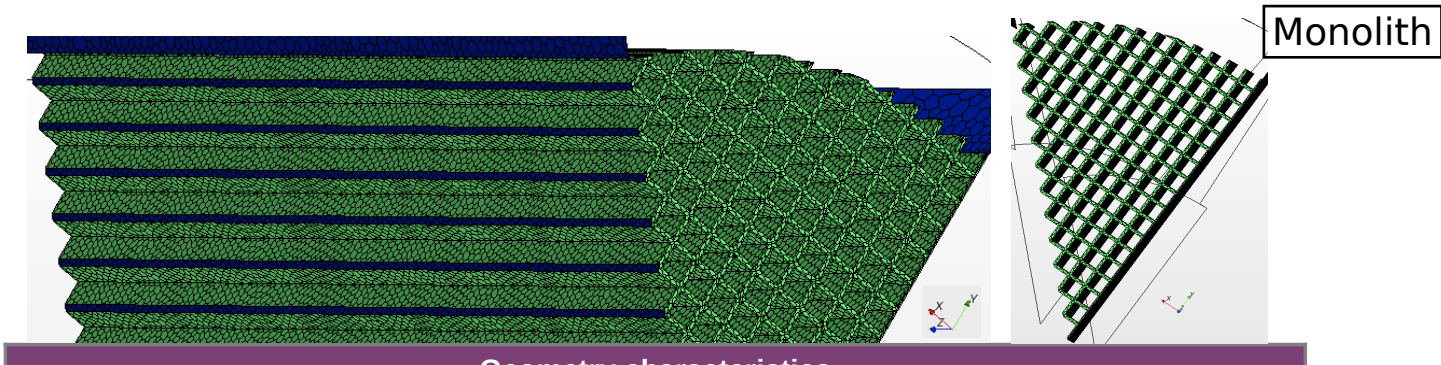

Global reformer		Monolith	
Simulated arc	45 deg	Fabricator	NGK
Total length	197,5 mm	Cell density	600 cpsi = 0,93 c/mm²
Max. diameter	42 mm	Void fraction	~ 70% (*)
Monolith length	30 mm	Mean pore diameter	0,867 mm
Monolith diameter	37 mm	Wall thickness	0,170 mm
(*) - In the second geometry's simulation the thickness of the monolith's wash-coat, 40microns, was added to the monolith's walls, resulting in a decrease of void fraction and consequent changes in mean pore diameter and wall thickness.			

Table 8: CPOx 2nd prototype – Geometry

3.3 Mesh

Polyhedral mesh with prismatic layers on each wall to account for the boundary layers and extrusions both at the inlet and the outlet.

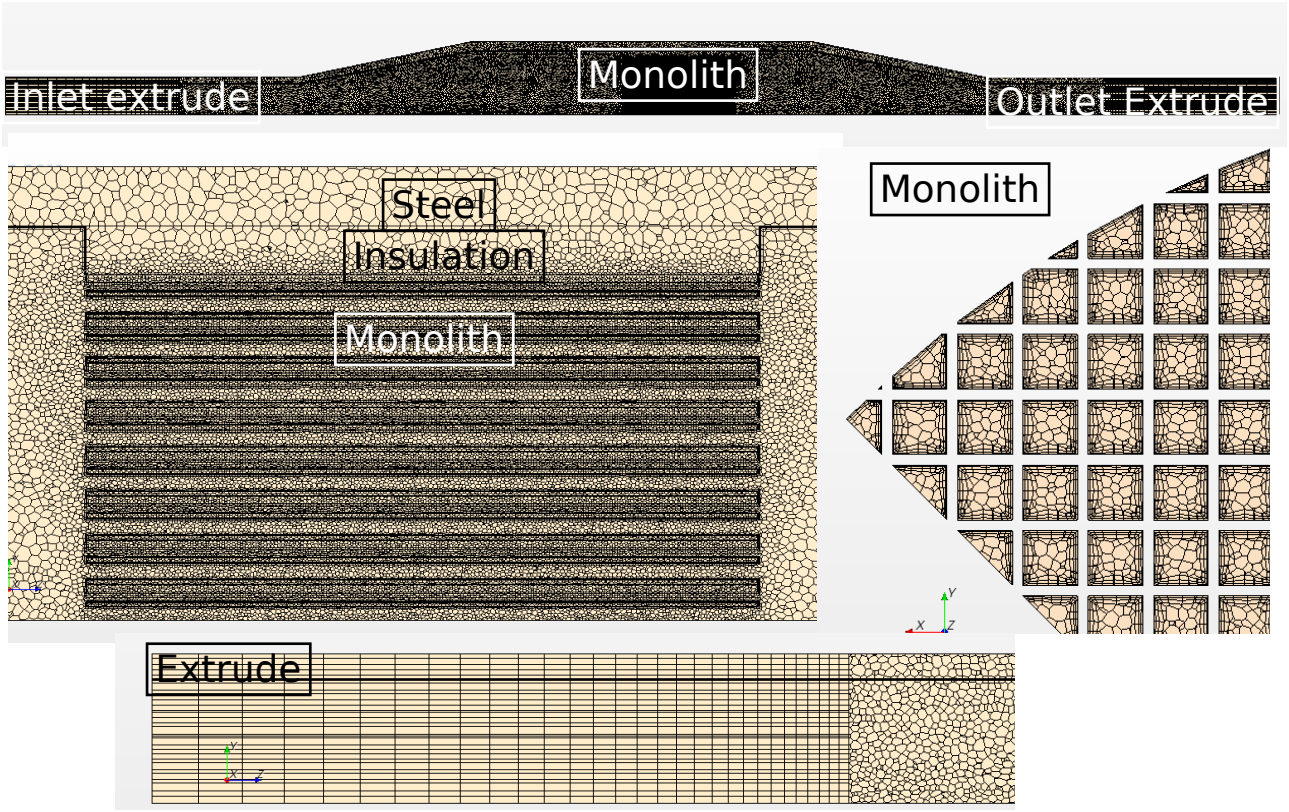

Figure 19: CPOx 2nd prototype – Mesh

Overall mesh characteristics	
Total number of cells	4,33 million
Maximum cell base size	0,5 mm
Minimum cell size	0,12 mm

Table 9: CPOx 2nd prototype – Mesh

3.4 Simulation conditions

3.4.1 CPOx Reformer working condition

The simulated working conditions are described in the following table. The corresponding fuel flow is 4Nl/min.

Simulated working conditions	
Inlet temperature	369 ºC
Total mass flow (360deg)	0,372 g/s
Inlet chemical composition	Air (N2, O2) + Methane, lambda = 0,33
Outlet chemical components	CH4, N2, H2, H2O, CO2, CO
Perfectly mixed gas at inlet	

Table 10: CPOx 2nd prototype – Work conditions

3.4.2 Numerical models

The models used on the runs are described in the following table.

Numerical models	
Time	Steady
Turbulence	Laminar
Energy	Segregated fluid temperature
Density	Ideal gas
Viscosity	5th-order temperature polynomial
Thermal conductivity	5th-order temperature polynomial
Combustion	Emulated through species mass sources
Solid (monolith, insulation and steel-tube)	Constant density + Segregated solid energy

Table 11: CPOx 2nd prototype – Numerical models

3.4.3 Assumed fields / Field imposition

J. Navalho's one-dimensional detailed chemistry simulation results were used to emulate combustion in the 3D simulation [1]. The components' profiles there obtained for the CPOx Reformer under the same working conditions were forced in the 3D simulation by inserting corresponding mass sources/wells for each chemical component in the zone where combustion takes place, that is approximately within the first centimetre inside the monolith's volume.

The temperature profile is not imposed since it is a consequence of enthalpy conservation – both 1D and 3D simulations are adiabatic. Thus, given that the energy conservation models are activated, temperature change throughout the Reformer is a consequence of chemical composition variation.

The following images present the mole fractions of CH4 and H2 along the longitudinal section of the reformer.

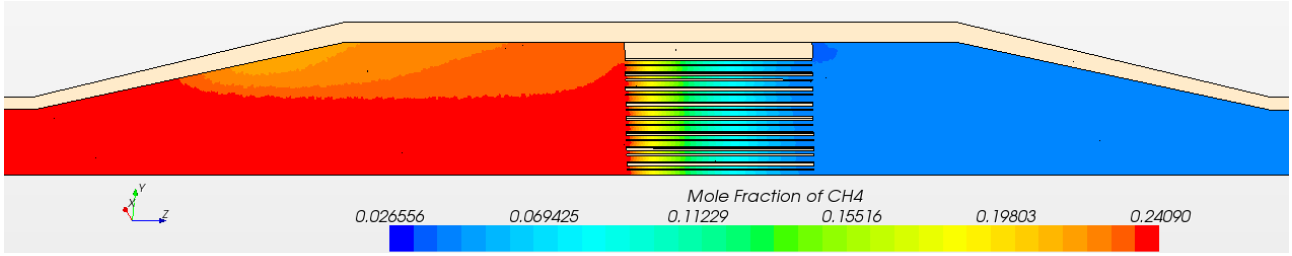

Figure 20: CPOx 2nd prototype – Molar fraction of methane

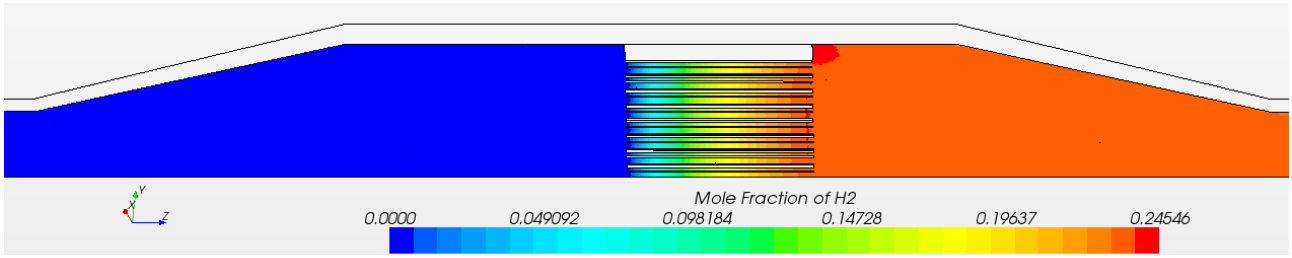

Figure 21: CPOx 2nd prototype – Molar fraction of hydrogen

The plot shows the obtained 3D profiles comparing to the 1D profiles imposed. Some differences occur in the transient zone due to 3D transport phenomena.

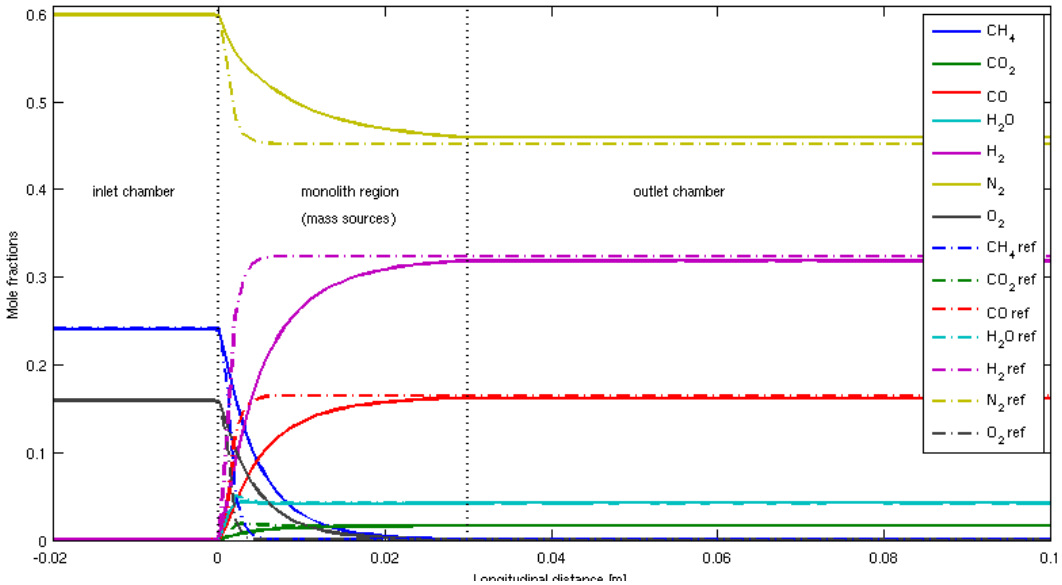

Plot 2: CPOx 2nd prototype – Molar fractions

3.5 Results

3.5.1 Reynolds number – Laminar flow regime

To confirm that the flow is laminar in all the domain, a detailed analysis of the Reynolds number in all the domain was made. The overall result is that the Reynolds number is below approximately 1500 in all the domain, confirming the hypothesis.

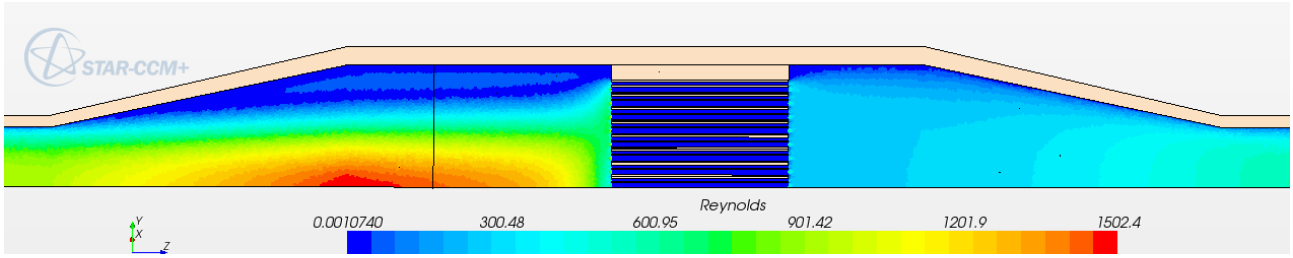

Figure 22: CPOx 2nd prototype – Reynolds

Reynolds number	
Maximum value in the domain	< 1503
Inlet	< 860
Monolith cells	~ 16

Table 12: CPOx 2nd prototype – Numerical models

3.5.2 Velocity field

The following image presents the vectorial velocity field on a longitudinal section across the Reformer. The plot below presents the area averaged velocity magnitude along several cross-sections along all the Reformer's length, complementing the picture.

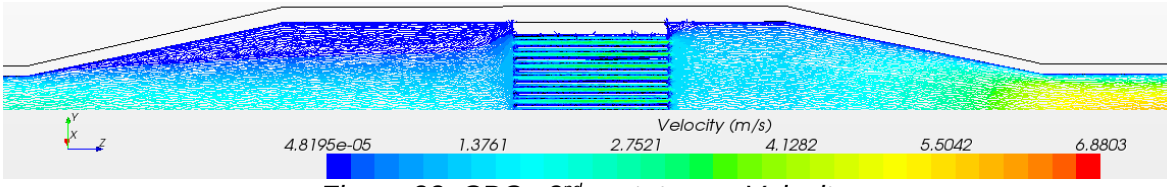

Figure 23: CPOx 2nd prototype – Velocity

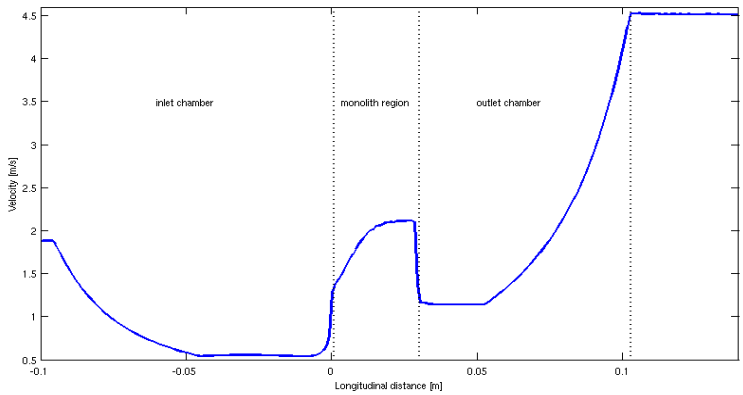

Plot 3: CPOx 2nd prototype – Velocity

Velocity variations inside the monolith region can be explained by variations of chemical composition and temperature inside it.

At the exit, velocity increases substantially because it's a high temperature flow reaching a compression cone region.

The image below shows the good distribution of flow in the monolith.

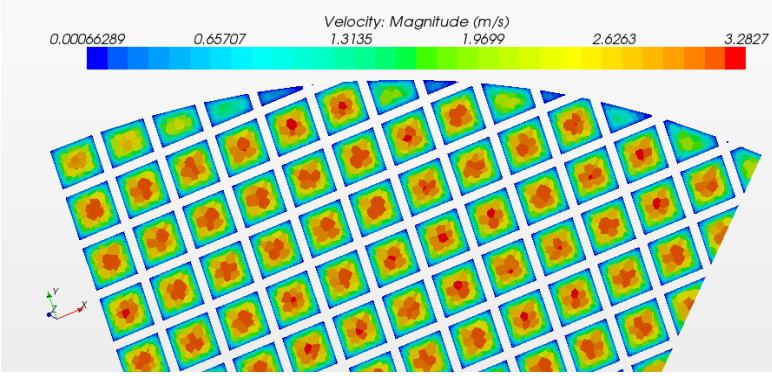

Figure 24: CPOx 2nd prototype – Velocity in the monolith

3.5.3 Streamlines

The inlet divergence angle for the CPOx Reformer's second prototype is 11,9 deg, even higher than in the first prototype, and also above the separation threshold for the current Reynolds number range.

The consequence is similar to that in the first prototype: a recirculation bubble is created acting like a wall on the flow. The following images present views of the streamlines evidencing the separated flow in the inlet chamber.

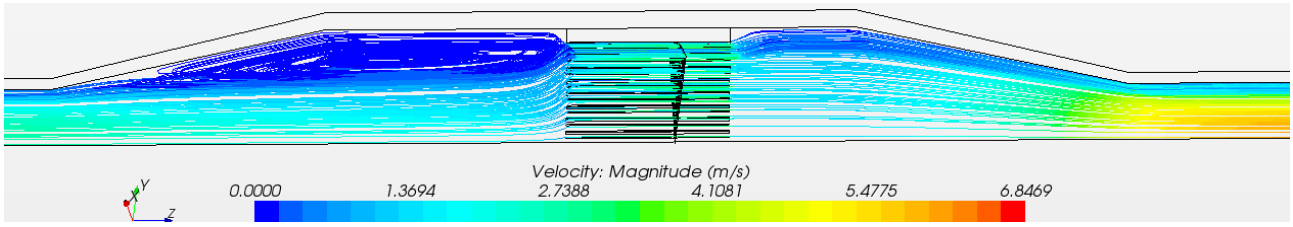

Figure 25: CPOx 2nd prototype – Streamlines

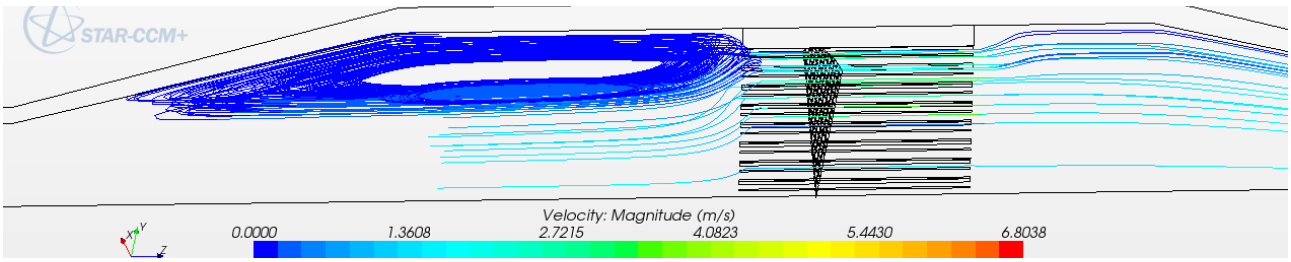

Figure 26: CPOx 2nd prototype – Streamlines – Separated flow

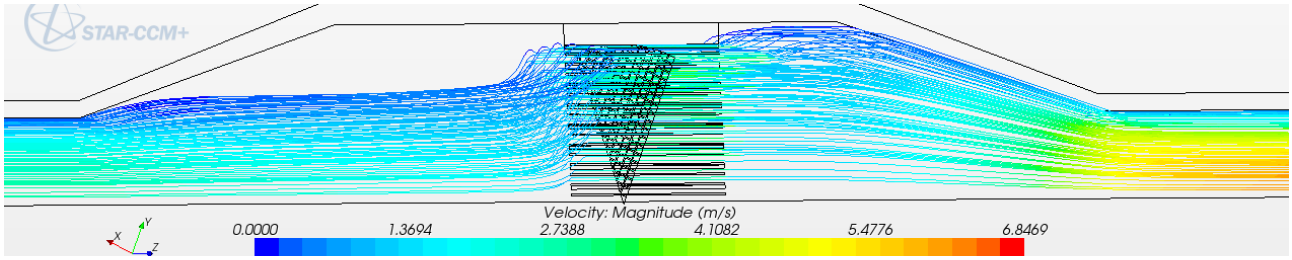

Figure 27: CPOx 2nd prototype – Streamlines – Main flow

3.5.4 Residence time

Another main consequence of the separated flow is, also as seen on the first prototype's simulation, that it dramatically increases the residence time of particles that enter it. The following images illustrate that.

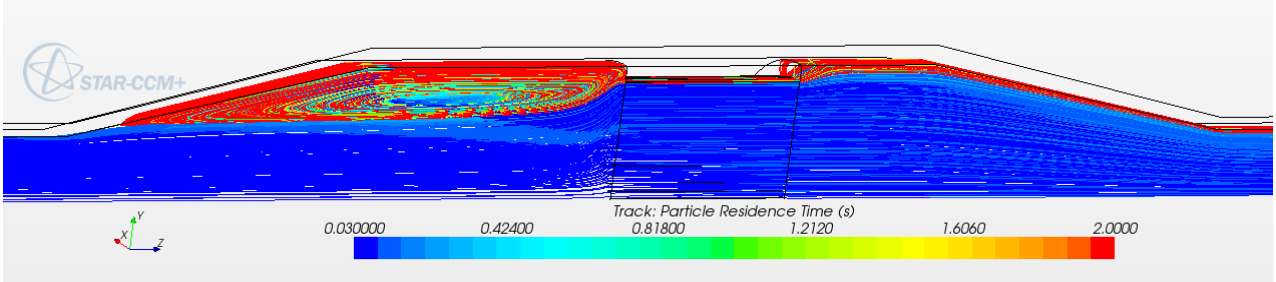

Figure 28: CPOx 2nd prototype – Residence time

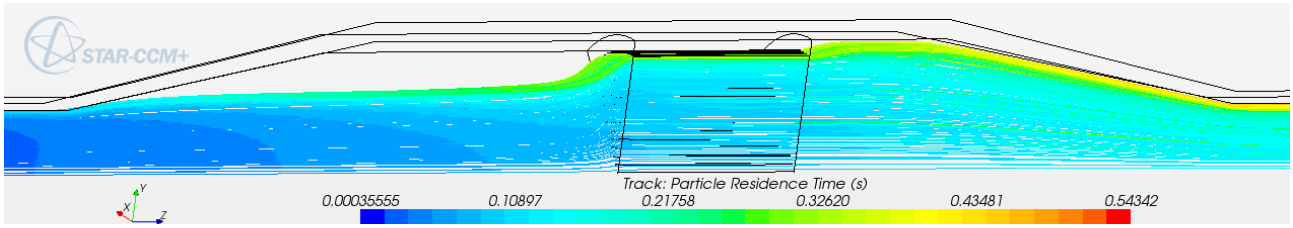

Figure 29: CPOx 2nd prototype – Residence time - Low

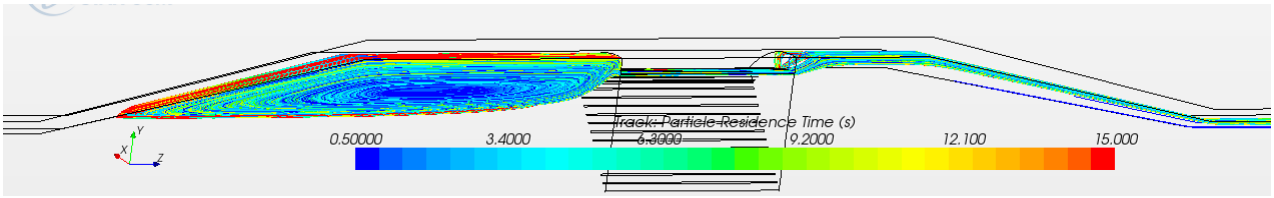

Figure 30: CPOx 2nd prototype – Residence time – High

For the second geometry case, the predicted residence times obtained are as follows.

Overall residence time	
Minimum (*)	0,10 s
Average	0,20 s
Maximum (*)	15 s
(*) - These values are estimations based on a random process analysis of particle path simulation.	

Table 13: CPOx 2nd prototype – Residence time

3.5.5 Temperature

As discussed above, the obtained temperature field is a direct consequence of how the 3D simulation followed the imposed mole fraction profiles.
Analysis of the plot below brings that the temperature follows imposed. An interesting note should be done to the increase of temperature in the recirculation bubble. That can be explained by the long time the particles within it are in contact with the hot steel-tube, giving them time to heat up. It

should also be noted although that this represents a small mass flow comparing to the mainstream, so the amount of fluid entering the monolith region already warm is not relevant.

The image and plot below show longitudinal views of the temperature field and the table shows overall results.

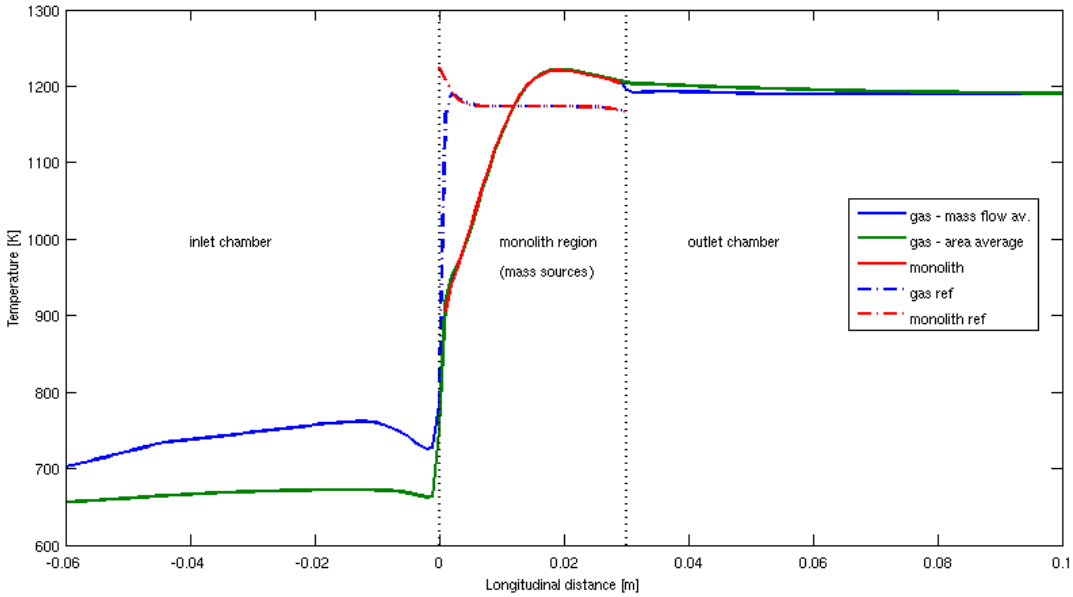

Plot 4: CPOx 2nd prototype – Temperature

Overall temperatures	3D simulation	1D simulation
Peak temperature	949 ºC	918 ºC
Monolith outlet temperature	930 ºC	893 ºC
Outlet temperature	917 ºC	-

Table 14: CPOx 2nd prototype – Temperature

3.5.6 Pressure

Overall predicted pressure drop through the Reformer is under 110Pa = 0,11mbar.

As expected the main pressure drop occurs in the monolith, being proportional to the mass flow and temperature of the fluid that crosses it.

The following image shows pressure along a longitudinal section of the Reformer; the plot shows the evolution of area-averaged pressure measured on cross-sections throughout the Reformer and the table shows the overall values.

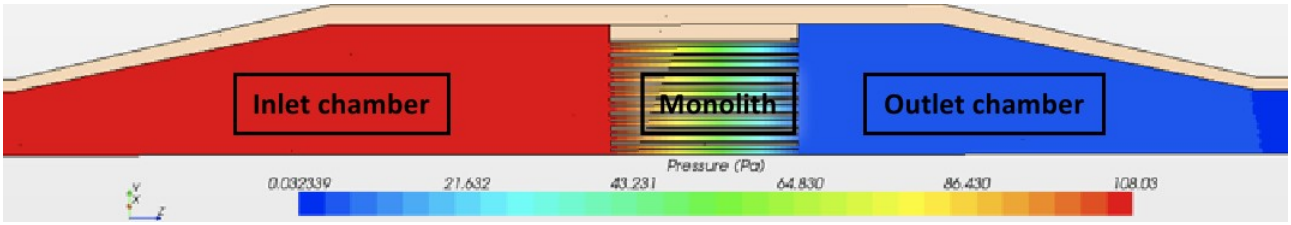

Figure 31: CPOx 2nd prototype – Pressure drop

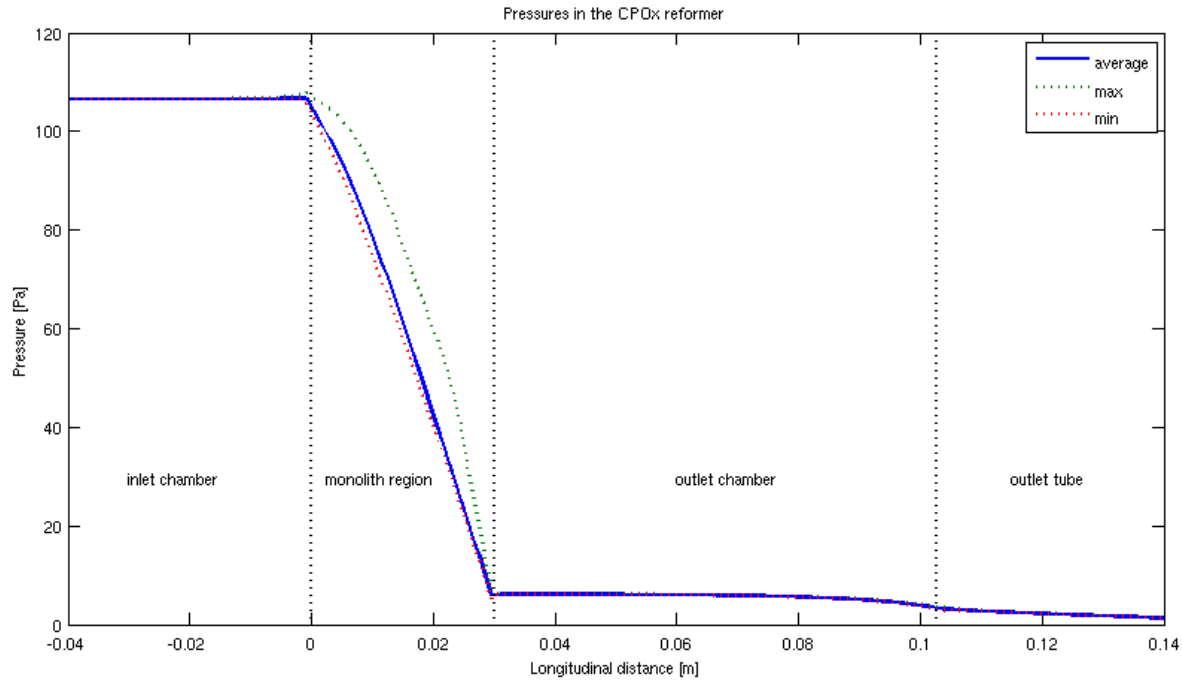

Plot 5: CPOx 2nd prototype – Pressure drop

Overall pressure drops	
Inlet chamber	~ 0 Pa
Monolith	~ 100 Pa
Outlet chamber	~ 3 Pa
Total pressure drop	< 110 Pa

Table 15: CPOx 2nd prototype – Pressure drop

3.6 Conclusions

There's a big recirculation bubble in the inlet chamber. It acts like a wall on the main flow stream and its main effect is to dramatically increase the residence time of the particles that enter it.
According to our results either the inlet chamber could be reduced in length or, otherwise, the divergence angle should be reduced to below 5deg to avoid the recirculation bubble.
This was taken into account while designing the third prototype, which has a divergence angle of 5deg in the inlet chamber.

4. CPOx Pre-heater (heat exchanger)

4.1 Introduction

A separate component for mixing the fuel and air streams before the CPOX reformer is necessary. EBZ suggested a configuration with an ejector pump at the inlet of the CPOX heat exchanger, as shown in the image below.
The fuel and air are mixed in the ejector and preheated with the afterburner exhaust gas in the CPOX heat exchanger. Hence, for the simulation of this component, it was divided into two distinct parts: the pre-mixer (Chapter 5) and afterwards the pre-heater or heat exchanger.

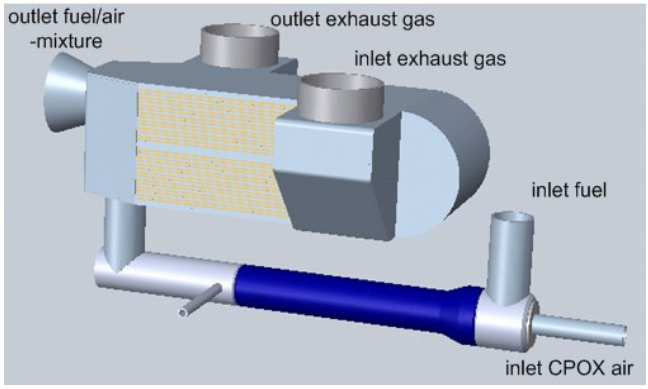

Figure 32: Heat exchanger – Prototype

The following simulations precede laboratory results and consist of a prediction of flow patterns, pressure drop and mixing/ heat exchange quality for each of the two sub-components.

4.2 Geometry

After separating the two components, the heat exchanger looks like the following image. The two streams exchange heat through the fine plates along their separate paths inside the heat exchanger.
General sizes are summarized in the table below.

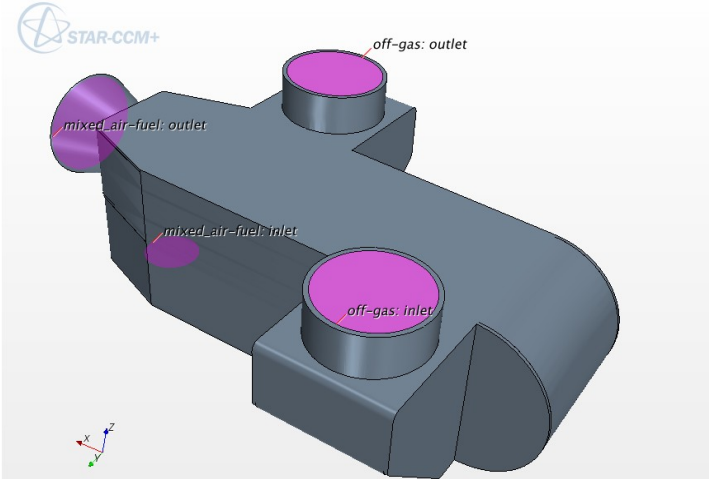

Figure 33: Heat exchanger – Simulated geometry

Geometry characteristics			
Global reformer		Monolith	
Cold Inlet diameter	24 mm	Box dimension	260 mm
Hot Inlet diameter	44 mm	Cold stream path length	479 mm
Cold Outlet diameter	40 mm	Hot stream path length	339 mm
Hot Outlet diameter	44 mm	Plates distance	1,00 mm

Table 16: Heat exchanger – Geometry

4.2.1 Cold stream – Mixed air+methane

The image below shows an upper view of the path of the cold stream, that will enter the CPOx reformer after heating up.

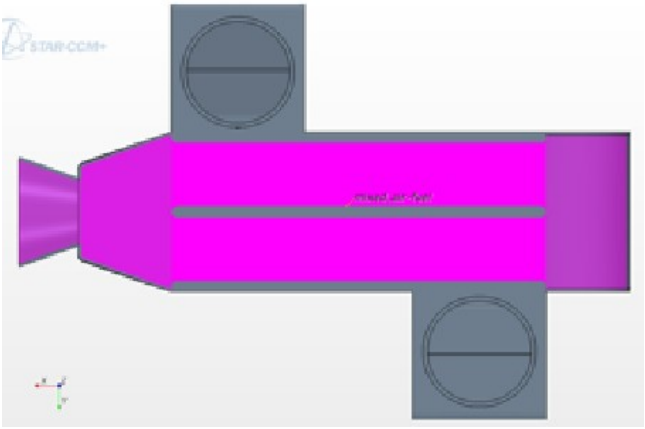

Figure 34: Heat exchanger – Cold stream

4.2.2 Hot stream – Burner offgas

The following image shows an upper view of the path of the hot stream, the offgas burner's combustion products used to heat up the CPOx reformer's fuel.

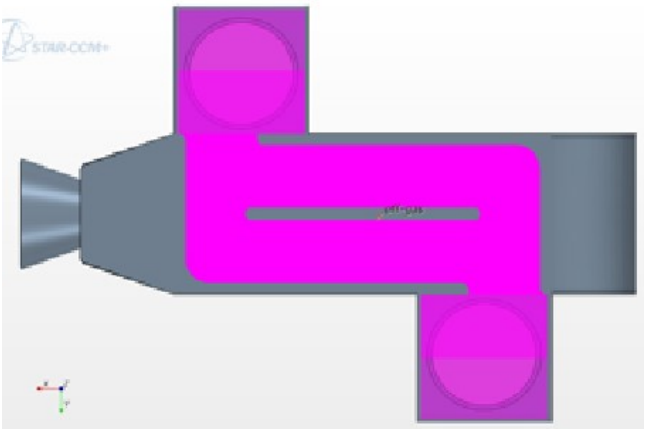

Figure 35: Heat exchanger – Hot stream

4.3 Mesh

Separate meshes were used for the solid and fluid phases. The solid mesh is a simple polyhedral mesh, whereas the fluid mesh is a combination of polyhedral cells with prismatic layer on the walls, extruder for the inlets and outlets and embedded thin mesher for the thin tubes that both fluids go through.

The following images show selected plane sections inside the heat exchanger highlighting some of the meshes' features.

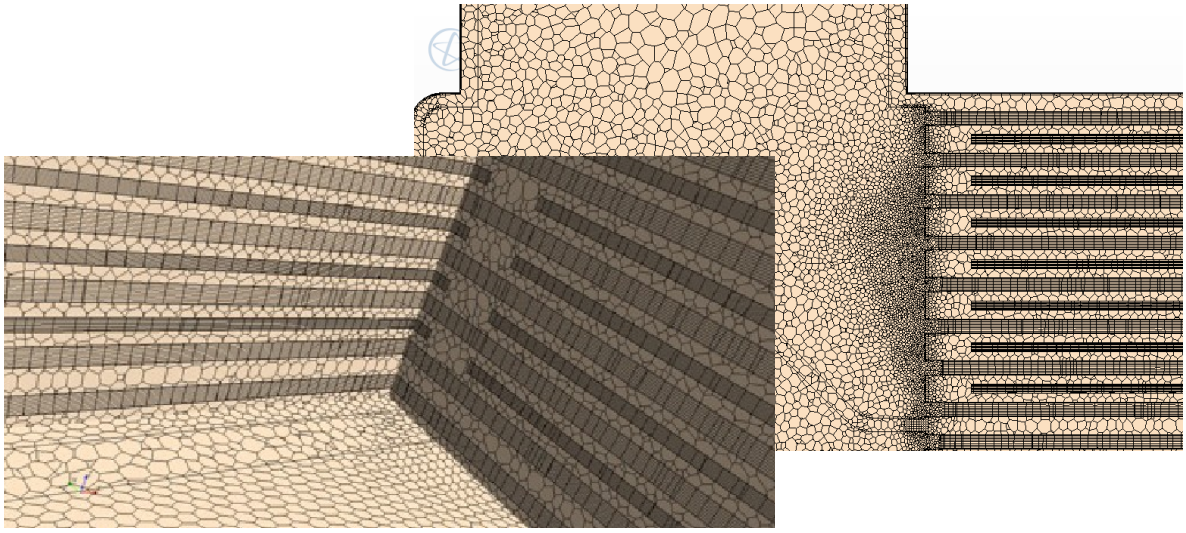

Figure 36: Heat exchanger – Mesh

The table summarizes general values regarding the mesh.

Overall mesh characteristics	
Total number of cells	11 million
Maximum cell base size	3,0 mm
Minimum cell size	0,6 mm
Thin mesher in tubes	10 layers

Table 17: Heat exchanger – Mesh

4.4 Simulation conditions

4.4.1 Heat Exchanger working condition

The working condition chosen for the heat exchanger's simulations was based on the so far simulated working conditions for the CPOx reformer and the Anode offgas burner. In this manner, the cold stream was defined as the inlet gas for the reformer and the hot stream was defined as the simulated combustion products from the offgas burner. The mixer component is assumed to provide a good mixing quality for the CPOx reformer fuel, so both streams are considered fully mixed at the heat exchanger inlet.
The table summarizes the simulated characteristics of both streams at the heat exchanger inlet.

Simulated working conditions		
	Cold stream	Hot stream
Inlet temperature	25 ºC	429 ºC
Mass flow	0,3172 g/s	4,848 g/s
Inlet fluid characteristics	Air (N2, O2) + Methane lambda = 0,33 Perfectly mixed gas	Cp = 1160,99 J/kg.K K = 0,0538 W/m.K miu = 3,267E-7 Pa.s

Table 18: Heat exchanger – Working conditions

4.4.2 Numerical models

The numerical models used for the runs are described in the following table.

Numerical models		
Fluid (both streams)	Time	Steady
	Turbulence	K-omega SST
	Energy	Segregated fluid temperature
	Density	Ideal gas
	Viscosity	5th-order temperature polynomial
	Thermal conductivity	5th-order temperature polynomial
Solid		Constant density + Segregated solid energy

Table 19: Heat exchanger – Numerical models

4.5 Results

4.5.1 Reynolds number – Flow regime

Analysis of the Reynolds number in key zones of the heat exchanger showed that for the simulated conditions the hot stream flow is mostly turbulent, as the cold stream is laminar.
Even though turbulent flow increases mixing quality, this should not be a problem because the mixer is predicted to provide a good mixing quality and also due to the length and complexity of the cold stream's path inside the heat exchanger.
The table below shows predicted Reynolds numbers values on key zones inside the heat exchanger.

Reynolds number		
	Cold stream	Hot stream
Inlet	869	4259
Outlet	154	4408
Tubes	15	29
Flow regime	Always laminar	Turbulent + Laminar

Table 20: Heat exchanger – Reynolds

4.5.2 Velocity field

Given the complexity of the heat exchanger's geometry, a global view of the velocity field is not possible. Hence some relevant detail areas are shown here.
Relevance is given to the separation occurring behind the directional plate between the two rows of plates (Figure below) as well as to the recirculation at the inlet, just before the flow enters the plates, as shown in the pictures below.

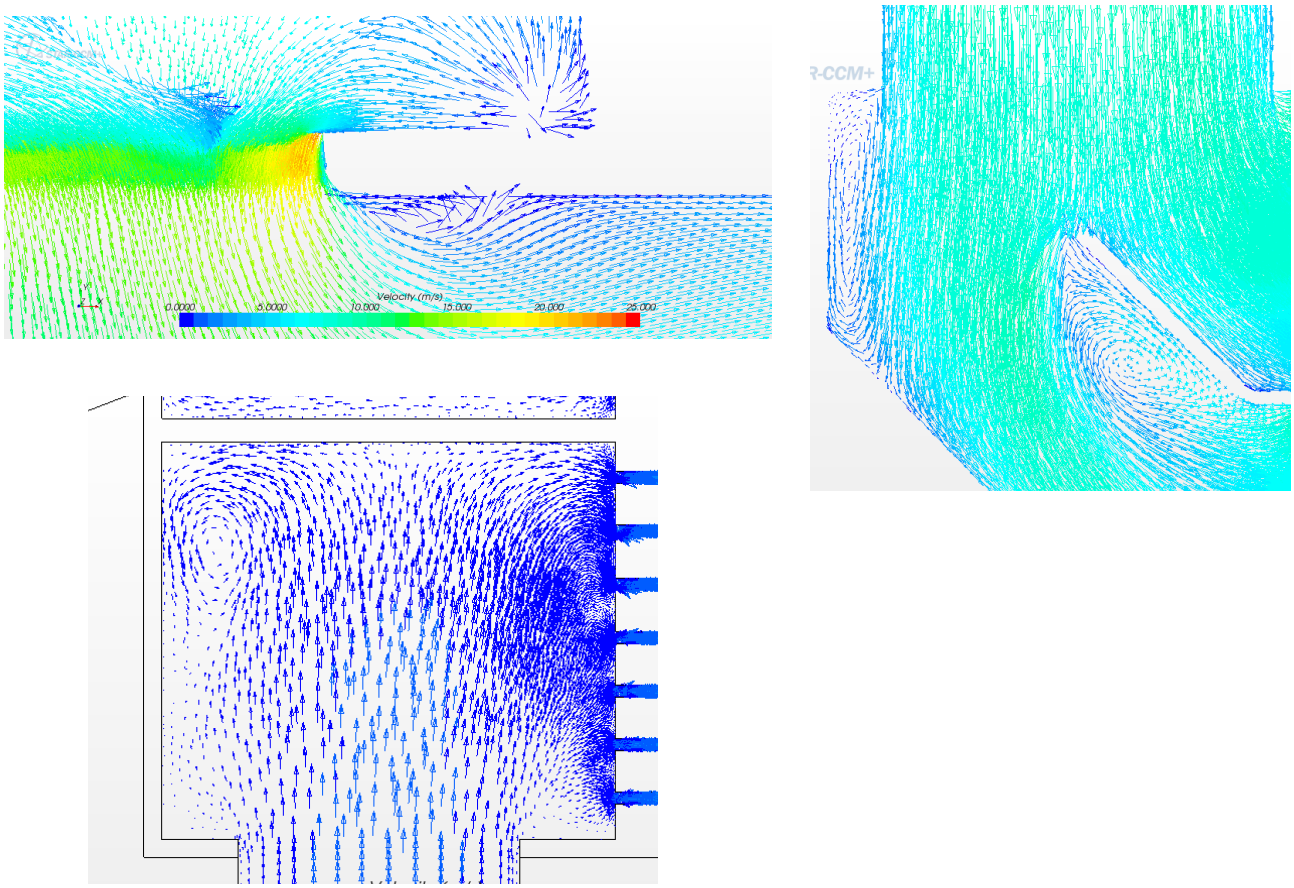

Figure 37: Heat exchanger – Velocity field – Details

4.5.3 Mass flow distribution in tubes

The distribution of flow between the parallel plates was analysed showing a difference in the two main plate areas, as is evident by the mass flows indicated in the picture below.
This unbalance is caused by a preferential path of the flow around the directional plate before the thin plates.

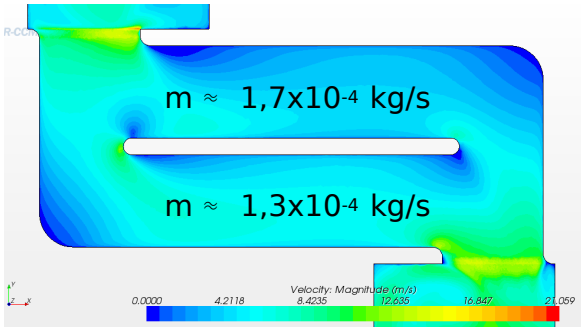

Figure 38: Heat exchanger – Mass flow distribution

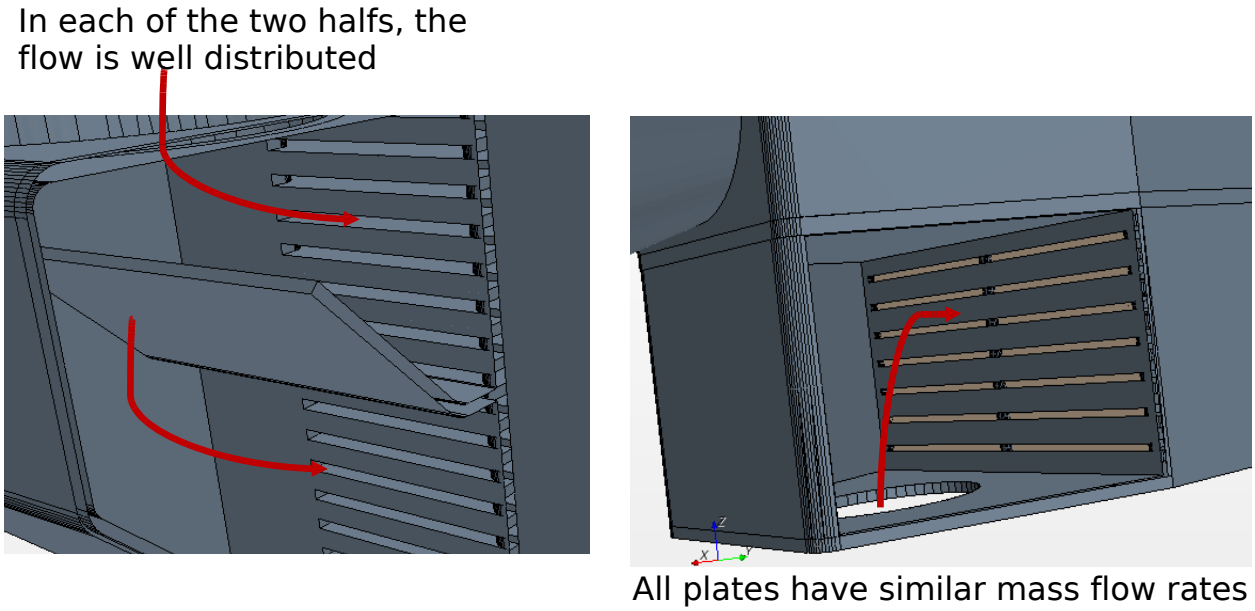

Figure 39: Heat exchanger – Mass flow distribution 2

4.5.4 Temperature

Temperature analysis shows that the flow streams have a 10ºC difference in temperature at the outlet.

An illustrative plot of temperature along a cross section of the heat exchanger is shown in the image below.

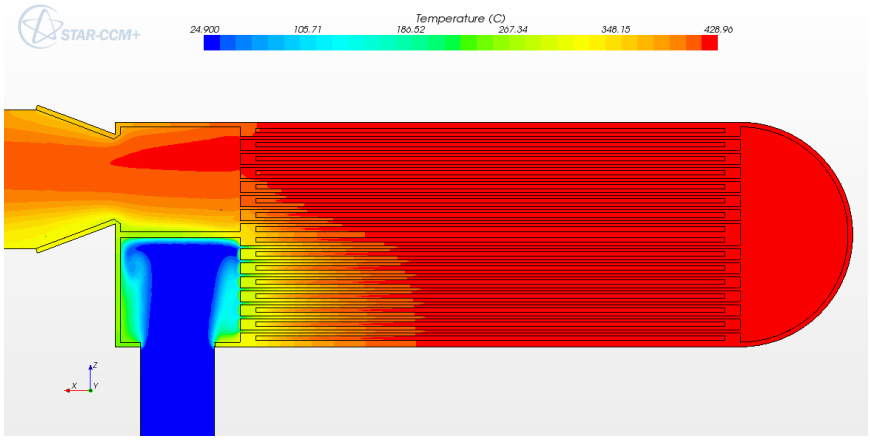

Figure 40: Heat exchanger – Temperature

The table outlines the outlet flow temperatures comparing to the global CHP working point.

Outlet temperatures	Cold stream	Hot stream
Working point expected	375 ºC	389 ºC
Simulated	391 ºC	401 ºC

Table 21: Heat exchanger – Temperatures

4.5.5 Pressure

Global pressure drops were computed. The results are shown below.

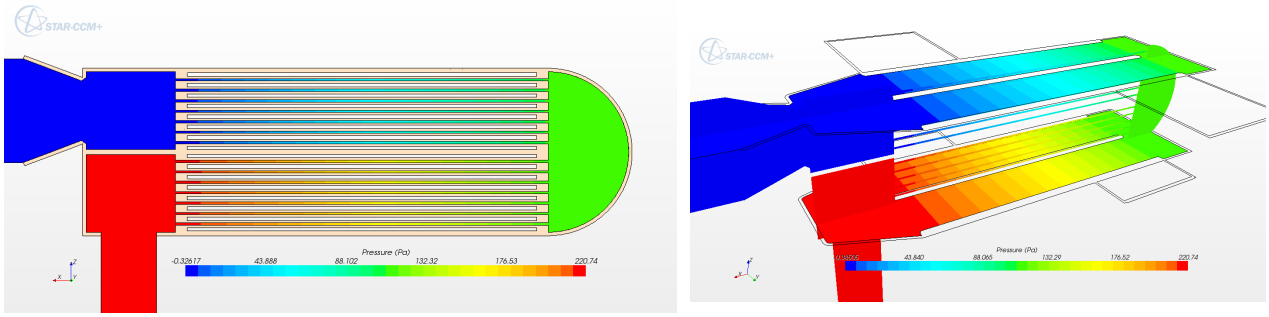

Figure 41: Heat exchanger – Pressure

Pressure drops	
Cold stream	2,23 mbar
Hot stream	4,2 mbar

Table 22: Heat exchanger – Pressure

4.6 Conclusions

The preliminary simulation results obtained for the heat exchanger show evidence of functioning within expected bounds, although improvement may be done, particularly with respect to pressure drops.

More simulations are under development in order to assess detailed results and specific suggestions.

5. CPOx pre-mixer

5.1 Introduction

The CPOx pre-mixer component is expected to provide good mixing between the air and fuel streams that are to enter the CPOx reformer while having a very little pressure drop.

5.2 Geometry

The mixer geometry suggested by EBZ consists of an ejector pump for the fuel inlet – air enters the mixer around the fuel stream – followed by a bottleneck and a static mixer. A more detailed image of the static mixer is shown below.

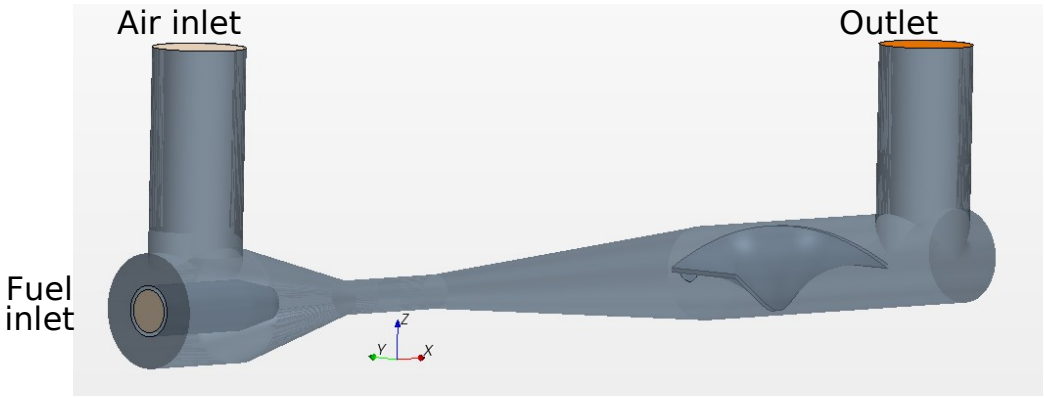

Figure 42: Mixer – Simulated geometry

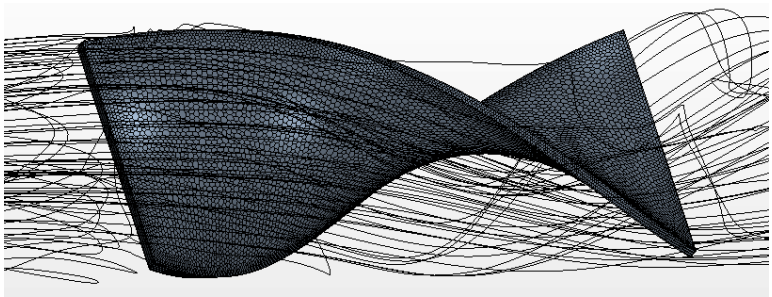

Figure 43: Mixer – Static mixer

Two similar geometries were simulated: the original geometry proposed by EBZ and a very similar geometry without the static mixer. The second geometry was simulated to assess the influence of the static mixer in the flow, with more emphasis on the pressure drop and mixing quality.

5.3 Mesh

A polyhedral mesh with prismatic layers on the walls to account for the boundary layers and extrusions both at the inlet and the outlet was used. Special refinement care was taken at the fuel

inlet and the static mixer. The following images show selected plane sections of the geometry highlighting relevant mesh features. The table below shows global measures of the mesh.

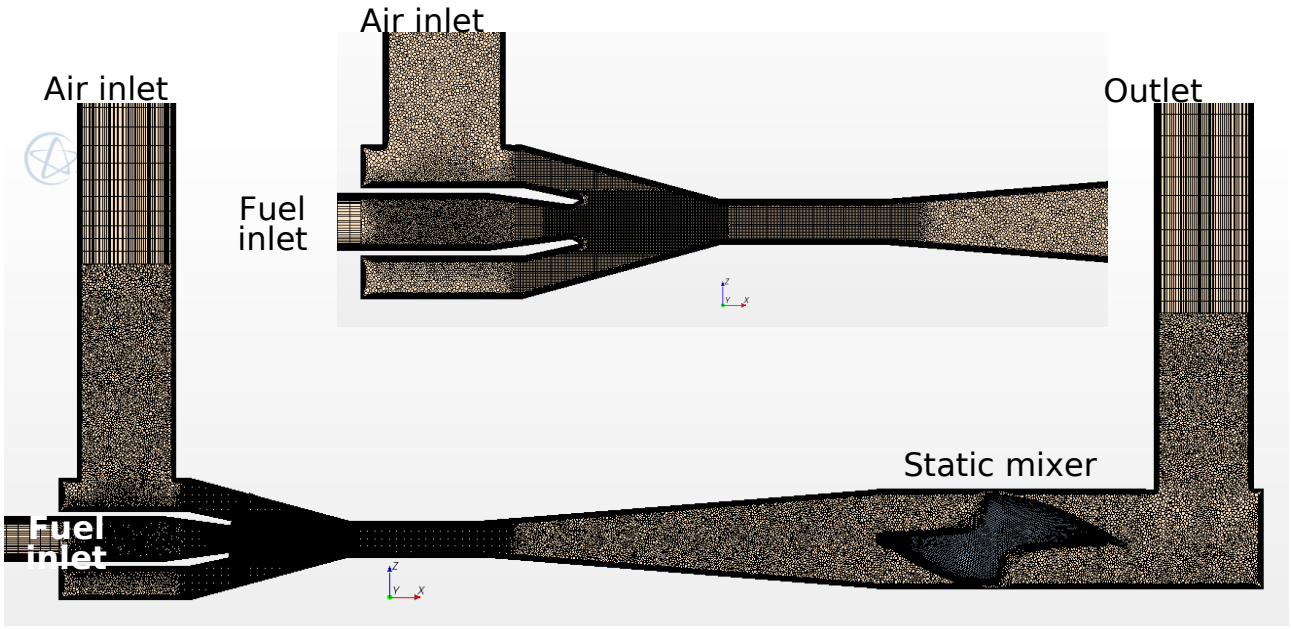

Figure 44: Mixer – Mesh

Overall mesh characteristics	
Total number of cells with static mixer	5,18 million
Total number of cells without static mixer	2,91 million
Maximum cell base size	0,5 mm
Minimum cell size	0,175 mm

Table 23: Mixer – Mesh

5.4 Simulation conditions

5.4.1 Working condition

The working condition under which the mixer was simulated corresponds to that under which the CPOx reformer was simulated. The mass flows and gas compositions are similar; differences reside in the temperatures – at the mixer the gas is still at room temperature – and the fact that the air and fuel are inserted in separate streams.
The table below describes the working condition.

Simulated working conditions	
Inlet temperature	25 ºC
Total mass flow	0,372 g/s
Inlet chemical compositions	Air (N2, O2) + Methane (CH4), lambda = 0,33

Table 24: Mixer – Working conditions

5.4.2 Numerical models

The simulation conditions used for the runs are described in the following table.

Numerical models	
Time	Steady / Unsteady
Turbulence	K-omega SST
Energy	Segregated fluid temperature
Density	5th-order temperature polynomial
Viscosity	5th-order temperature polynomial
Solid	Not simulated

Table 25: Mixer – Numerical models

5.5 Results with static mixer

5.5.1 Reynolds number / Flow regime

Flow inside the mixer is mostly turbulent for the current working condition.

Reynolds number	
Maximum value (in the throat)	~ 6800
Air inlet	~ 2450
Fuel inlet	~ 1240

Table 26: Mixer – Reynolds

5.5.2 Velocity field

The following images show two perpendicular longitudinal sections of the mixer. There is evidence of a preferential path around the static mixer inducing swirl in the flow.

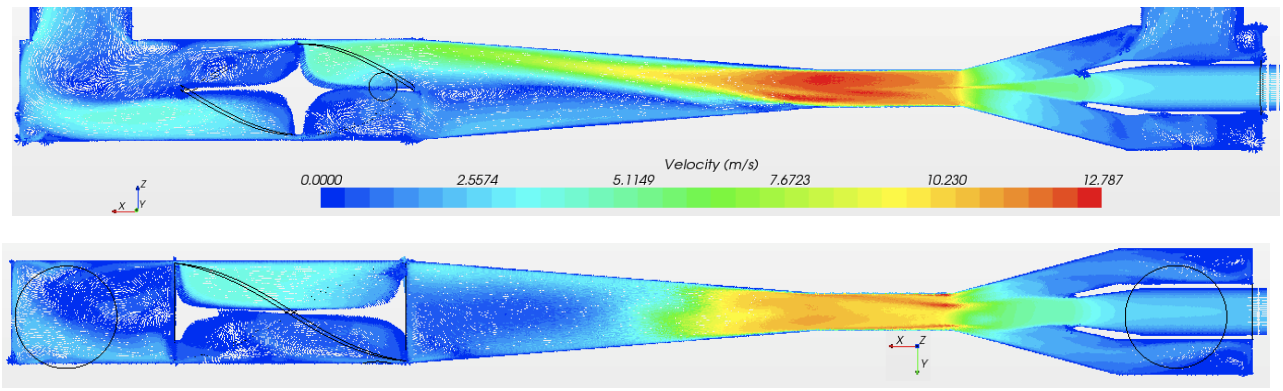

Figure 45: Mixer – Velocity

5.5.3 Streamlines

Analysis of the streamlines confirms the preferential path around the static mixer: most of the streamlines, hence most of the mass flow, contours the static mixer from one of its sides.

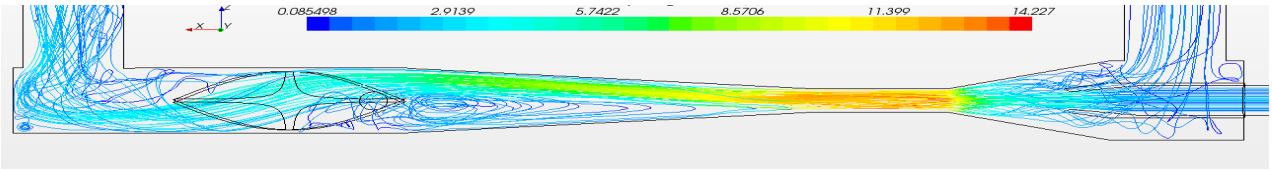

Figure 46: Mixer – Streamlines

5.5.4 Mixture quality

For the working conditions studied the mixer is effective. At the outlet the mass fraction of fuel is bounded between 0,155 ± 4,5%.

The image below to the left shows a longitudinal section of the mass fraction of fuel. The image to the right shows three cross-sections: before the static mixer, after the static mixer and the at the outlet. This image serves to demonstrate that the static mixer has a little effect on the final mixing quality.

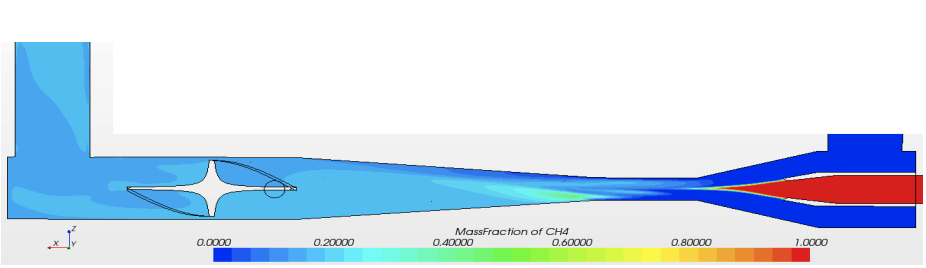

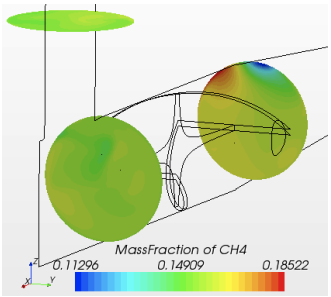

Figure 47: Mixer – Mixture quality

5.5.5 Pressure

The predicted pressure drop inside the mixer is of 0,61mbar.

The image below shows a longitudinal section of the pressure along the mixer.

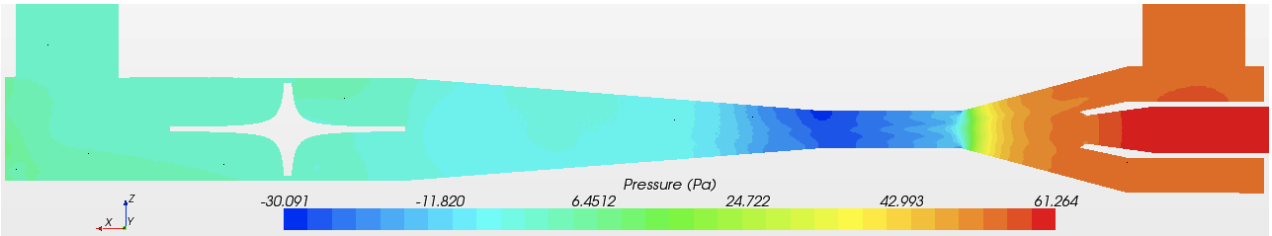

Figure 48: Mixer – Pressure drop

5.6 Results without static mixer

5.6.1 Reynolds number / Flow regime

Flow inside the mixer is mostly turbulent for the current working condition.

Reynolds number	
Maximum value (in the throat)	~ 5670
Air inlet	~ 3040
Fuel inlet	~ 1235

Table 27: Alternative mixer – Reynolds

5.6.2 Velocity field

The velocity field without the static mixer is also asymmetric and has a separation region. This is expected given the high velocity in the expansion region. An image of the relevant longitudinal section is below.

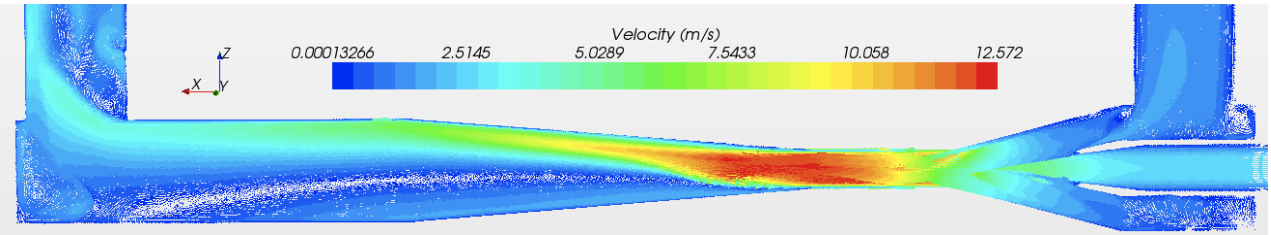

Figure 49: Alternative mixer – Velocity

5.6.3 Streamlines

The previously mentioned asymmetry of the flow and the separation regions are more apparent in the image below, that shows the flow streamlines. Two separation bubbles are easily distinguished as well as a strong swirl at the exit.
The flow in the mixer without static mixer is very similar to that of the original geometry, with the static mixer.

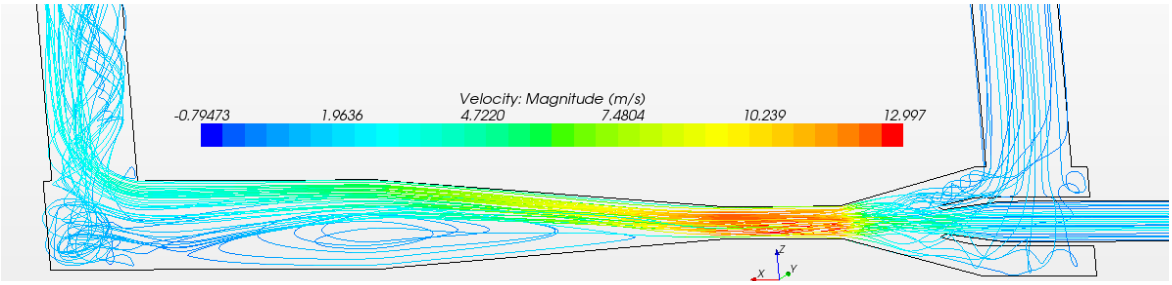

Figure 50: Alternative mixer – Streamlines

5.6.4 Mixture quality

The static mixer is proven to not have an important effect on the mixing quality. The mixing quality predicted for both geometries – with and without static mixer – is similar as the mass fraction of fuel at the outlet is bounded between the same values in both geometries.
The images below compare to those shown before for the original geometry containing the static mixer. No significant difference in the mixing quality can be observed.

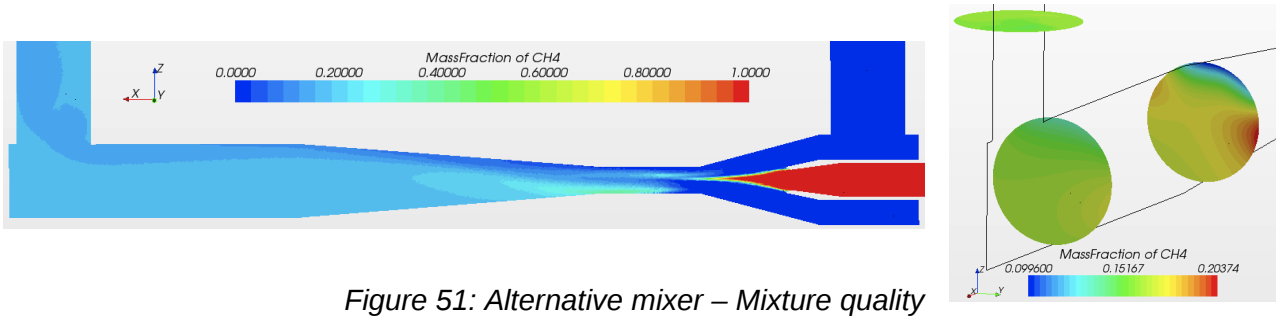

Figure 51: Alternative mixer – Mixture quality

5.6.5 Pressure

The absence of the static mixer brings a small reduction on the pressure loss. In the alternative geometry the overall pressure loss is about 0,60mbar, approximately 1Pa less than the original geometry. This difference is not very significant.

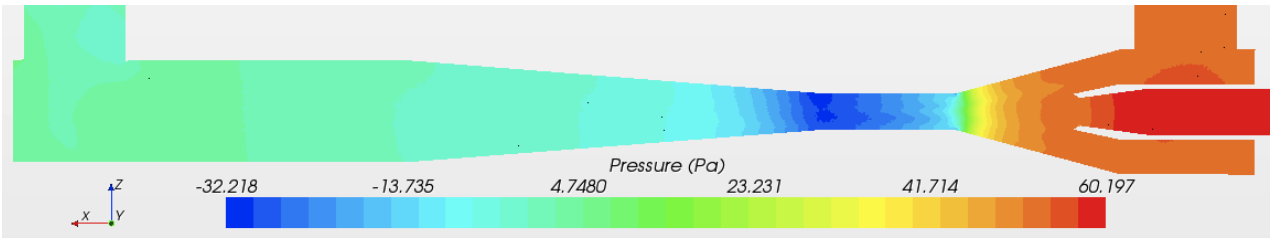

Figure 52: Alternative mixer – Pressure drop

5.7 Conclusions

The mixer component is effective. Both with and without the static mixer inside the mass fraction of fuel at the outlet was predicted to be bounded between the same values.
Hence, the static mixer is ineffective since it doesn't affect the flow nor the mixing quality. It was only observed that the outlet swirl is more intense in the presence of the static mixer.

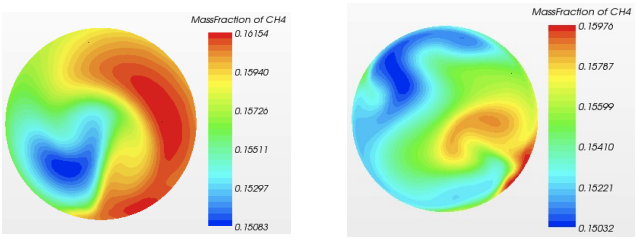

Figure 53: Mixer – Mixture quality comparison

The observed flow separation region was also not induced by the static mixer. Given the high velocity characteristics of the simulated working conditions, it's not possible to extrapolate this result to lower mass flows, that is, flows with lower velocity.

6. 1D Numerical Simulations

6.1 Physical and mathematical model

One dimensional numerical simulations were performed using a heterogeneous mathematical model for a single channel of the entire honeycomb monolith. The model developed assumes no heat and mass transfer across channel walls which is a good assumption when the incoming feed stream properties are uniformly distributed over all channels at the catalyst inlet section and when the thermo-physical properties of the substrate and washcoat support as well as the catalytic distribution along the axial direction is uniform for all channels. This means fundamentally that fulfilling these conditions all channels operate under identical conditions.

Indeed this kind of modelling approach, having its simplifications, is widely used in literature, instead of the complete 3 dimensional multi-channel modelling approach because it gives a good ratio between its results and the related computational costs. Therefore, concerning parametric studies, this kind of modeling approach is an optimal choice.

Being heterogeneous the model treats the reactor behaviour with two distinct phases, the bulk gas phase and the solid phase, and energy and mass balances are performed for each phase.
Hence, the model can predict the temperature and the product distribution of the bulk gas phase along the axial direction of the monolith and the temperature achieved in the catalyst surface, where the catalytic heterogeneous reactions are accounted, as well as the composition of the thin boundary layer that fills the washcoat pore structure. Both phases are coupled together by heat and mass external transport properties based on *Nusselt* and *Sherwood* correlations respectively, suitable for the geometrical properties of the catalyst carrier and the range of working conditions.

The governing equation for species and heat balances for each phase are presented bellow. Although this work is only interested in steady-state conditions, the dynamic terms are also shown for the sake of completeness. Each term is written on a total reactor volume.

Gas Phase Balance Equations

Mass Balance Equation

$$\epsilon\rho_g\frac{\partial Y_{k,g}}{\partial t}+\epsilon\rho_g u\frac{\partial Y_{k,g}}{\partial x}+\frac{\partial}{\partial x}\left(\rho_g\phi Y_{k,g}V_{k,g}\right)+a_V\rho_g K_{mat,k}(Y_{k,g}-Y_{k,w})=0$$

Energy Balance Equation

$$\epsilon\rho_g C_{p,g}\frac{\partial T_g}{\partial t}+\epsilon\rho_g C_{p,g}u\frac{\partial T_g}{\partial x}-\frac{\partial}{\partial x}\left(\epsilon\lambda_g\frac{\partial T_g}{\partial x}\right)+a_V h(T_g-T_s)=0$$

Solid Phase Balance Equations

Mass Balance Equation

$$\rho_{bl}\frac{\partial Y_{k,w}}{\partial t} - a_V \rho_{bl} K_{mat,k}(Y_{k,g} - Y_{k,w}) - \dot{\omega}_{k,w} W_k = 0$$

Energy Balance Equation

$$(1-\epsilon)\rho_s C_{p,s}\frac{\partial T_s}{\partial t} - \frac{\partial}{\partial x}\left(k_{s,eff}\frac{\partial T_s}{\partial x}\right) - a_V h(T_g - T_s) + \sum_{k=1}^{KK_w}\dot{\omega}_{k,w}H_k = 0$$

Owing to the relative small *Peclet* numbers, molecular and heat diffusion were accounted for in the bulk gas phase equations. Radiative heat transfer inside monolith channels can be easily handled in this model using a radiative contribution on the effective solid thermal conductivity:

$$k_{s,eff} = k_s(1-\epsilon) + k_r$$

The last term is the radiative contribution given by *Lee* and *Aris* correlation [3] for monolithic reactors:

$$k_r = \frac{16}{3}\sigma(d_h/2)T_s^3\psi(\chi)$$

Given that catalytic partial oxidation of hydrocarbons occurs primarily at the catalytic surfaces of the reactor, the chemical kinetics contribution of CPOx was accounted for on the solid phase balances. It follows a proper heterogeneous reaction mechanism considered to describe the chemical pathway from reactants to products that occurs in the catalytic active sites, at the channel walls. We have used several reaction mechanisms for methane CPOx either global or detailed. Global mechanisms for heterogeneous catalytic reactions usually follow the *Langmuir-Hinshelwood* type of rate equations whereas for detailed multi-step reaction mechanisms the use of *power-law* type of rate equations is much more usual with some modifications, namely the coverage dependence on the pre-exponential factor and the activation energy.

Since in a porous catalyst the reactions occur inside the pores, the reactant species must diffuse from the interface between bulk gas flow and the catalyst surface through the pore structure. While the species are diffusing some of them react and sharp concentration gradients can occur along the washcoat especially when the intrinsic kinetics is very fast. Thus under relative thick washcoats the internal diffusive resistances of reactant species along the pore structure can play an important role, limiting the rate of conversion of reactants. This transport phenomenon is also taken into account for modeling purposes through isothermal effectiveness factors using Thiele modulus:

$$\eta_{Ri} = \frac{tanh(\phi_{k,Ri})}{\phi_{k,Ri}}$$

This approach to overcome the internal diffusive limitation is usually preferred instead of the detailed model solution of the differential reaction-diffusion equation along washcoat normal direction because the computational time required for this method is much lower than that using the detailed description.

Following literature results [4-5], gas phase reactions were not considered in the model scheme because at typical CPOx conditions (atmospheric pressure and millisecond contact times) the heterogeneous reactions contribution on feed stream conversion is much more important than the contribution from gas phase reactions. However, homogeneous reactions become important at pressures higher than 5 bar [6-7].

For details about transport properties or reaction mechanisms used up to now for methane CPOx over PGM catalysts, please find an earlier technical report uploaded at EMDESK [8].

6.2 Numerical model

The governing equations shown above were implemented in an in-house CHEMKIN based code with finite difference approximation method that reduces the differential equations to a system of algebraic equations. Thus:

- - Convective terms were discretized with first-order upwind schemes;
- - Diffusion terms were discretized with second-order central differences.

Therefore, to solve the system of nonlinear equations, a modified Newton method was used and an adaptive mesh procedure was applied based on two adaptive criteria: gradients and curvatures of all dependent variables between each mesh point must be kept bellow a user specified value.

A time-step procedure is used to find the steady-state solution of all variables and therefore an accurate initial guess for the solution is not required.

For detailed multi-step surface reaction mechanisms the open source code CANTERA was adapted and coupled with the main code to deal with chemical kinetics. CANTERA was chosen as a kinetic interpreter for heterogeneous reactions, reading microkinetic models written in standard CHEMKIN format and returning to the main code the kinetic source terms needed to solve both solid phase balance equations.

6.3 Validation

The model developed was successfully validated against experimental data reported in literature. Only one of the cases used for validation is shown here. The case presented on this section uses the governing equations as described above and uses a global reaction mechanism for methane CPOx on Rhodium [9]. This mechanism comprises 6 chemical species (CH_4, O_2, CO_2, H_2O, H_2 and CO) and follows an indirect kinetic scheme of syngas production: syngas is just created after the beginning of the total oxidation of the fuel. Hence, this mechanism includes 6 global reactions: methane total oxidation (highly exothermic) which produces H_2O, followed by methane steam reforming (highly endothermic) which consumes the remaining methane with the H_2O produced

previously, direct and reverse WGS, and consecutive oxidation of CO and H2. Dry reforming reaction is out of this methane CPOx reaction scheme following some literature results [10].

The reactor (Figure 54), is composed by a 400 cpsi honeycomb monolith with square channels and with a washcoat (4% wtRhα -Al2O3) between two inert foams acting as heat shields. The benchmark used to validate results from numerical implementation of the model and the reaction mechanism can be found in [11].

The computational domain comprises the inlet section of the first foam (x=-1.5cm) and ends at the outlet section of the second foam (x=3.5cm).

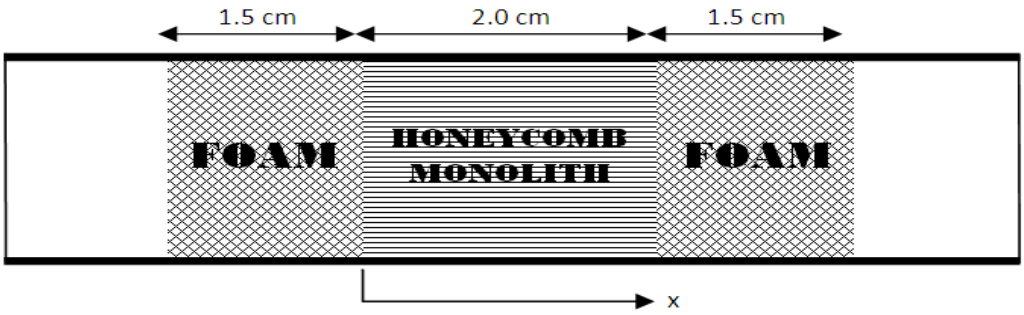

Figure 54: Reactor layout

The catalyst section corresponds to the honeycomb monolith region. As described above, the remaining regions are inert and just act as a radiation heat shield to ensure negligible heat losses in axial direction.

The boundary conditions applied to the governing equations are presented bellow.

Reactor Inlet $(x = -1.5cm)$

$$Y_{k,g} = Y_{g,in}$$

$$T_g = T_{g,in}$$

$$\frac{\partial T_s}{\partial x} = 0$$

Reactor Outlet $(x = 3.5cm)$

$$\frac{\partial Y_{k,g}}{\partial x} = 0$$

$$\frac{\partial T_g}{\partial x} = 0$$

$$\frac{\partial T_s}{\partial x} = 0$$

Next figure presents the operating condition used in numerical simulations and in experimental procedures [11].

	$T_{g,in}$	$546\ K$
	P	$1\ atm$
$X_{g,in}$	X_{CH_4}	0.2735
	X_{O_2}	0.1473
	X_{N_2}	0.5792
	λ	0.27
	$\dot{m}$	$0.18\ g/s$

Figure 55: Working condition

In the next figures the model results for temperature profiles and product distribution of the species considered by the reaction mechanism are shown.

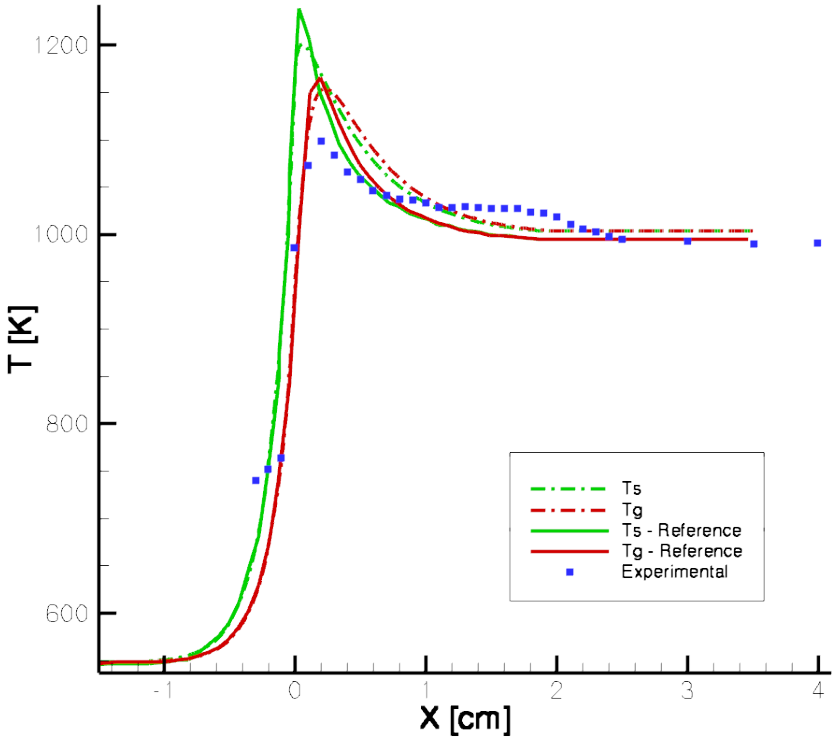

Figure 56: Thermal profiles obtained (Ts - solid and Tg – bulk gas) with benchmark data (Reference: profiles obtained with a similar model approach; Experimental: Data collected experimentally for gas temperature)

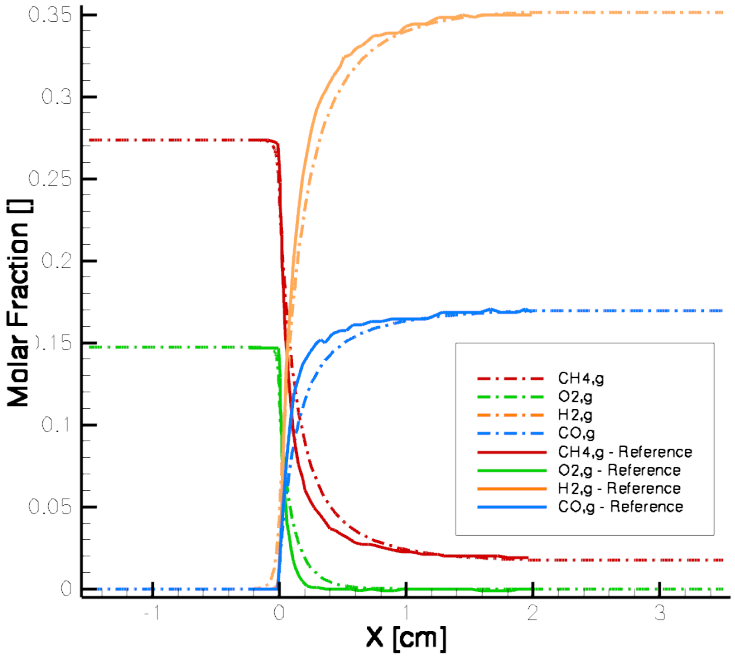

Figure 57: Species profiles obtained (reactant species and species associated to partial oxidation scheme) and benchmark data (Reference: profiles obtained with a similar model approach)

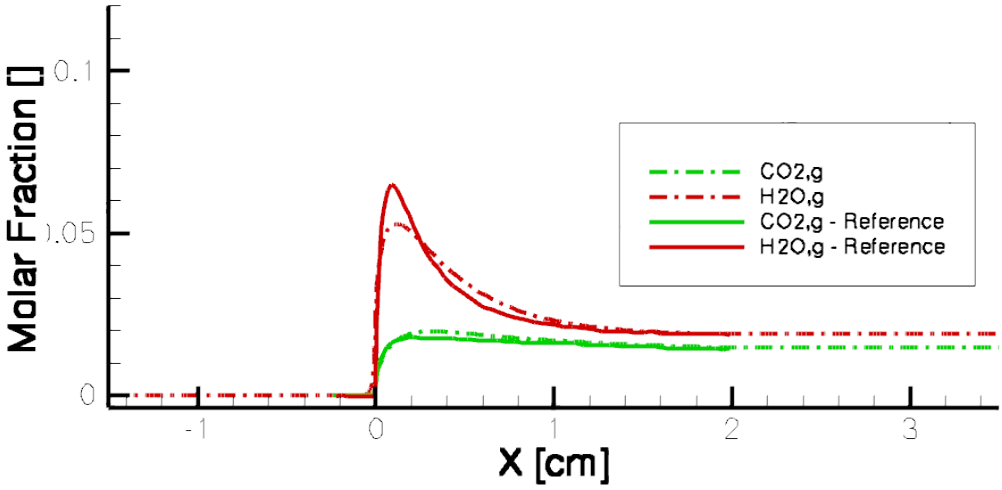

Figure 58: Species profiles obtained (species associated to total oxidation scheme) and benchmark data (Reference: profiles obtained with a similar model approach)

The implementation of the present model, as one can see, returns results very close to those considered as benchmark.

In the next plots the species profiles for the bulk gas flow (denoted by *g*) and for the boundary layer that surrounds the catalysts surface (denoted by *w*) are shown.

Note that species that are being consumed in each section present a lower molar fraction in the boundary layer (*w*) than in the bulk gas flow (*g*) (Figure 59), whereas species that are being produced (like hydrogen or carbon monoxide – Figure 61) present a higher molar fraction in the boundary layer.

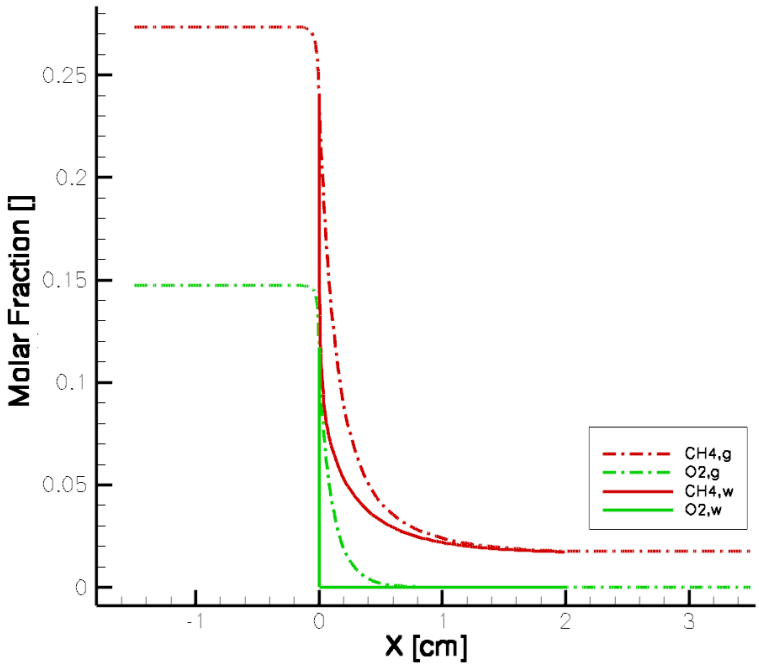

Figure 59: Species profiles of methane and oxygen for both phases

Looking at Figure 59, it is clear that at the catalyst entrance (x=0.0cm) there are strong transport limitations due to the fast kinetics in this region. The oxygen fraction contained in feed flow stream is completely consumed in the first 1 cm of the catalyst. The strong consumption of both reactants follows the total oxidation stoichiometry and is responsible for the huge heat released in the

catalyst inlet section. However, from the arising of H2O and CO2 (Figure) steam reforming reaction starts to gain importance consuming energy previously released and lowering the surface temperature of the catalyst.

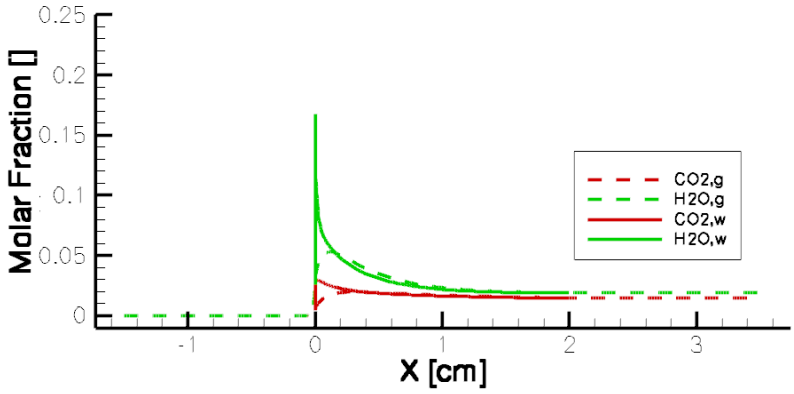

Figure 60: Species profiles of carbon dioxide and water for both phases

In Figure 60, one can see that at the first millimeters water changes from product to reactant for steam reforming reaction. In the section where both profiles of H2O cross (about 0.2cm) steam reforming starts to consume water already in the bulk gas flow. Concerning the CO2 profiles, it became clear that CO2 reforming does not play a major role in the overall process.

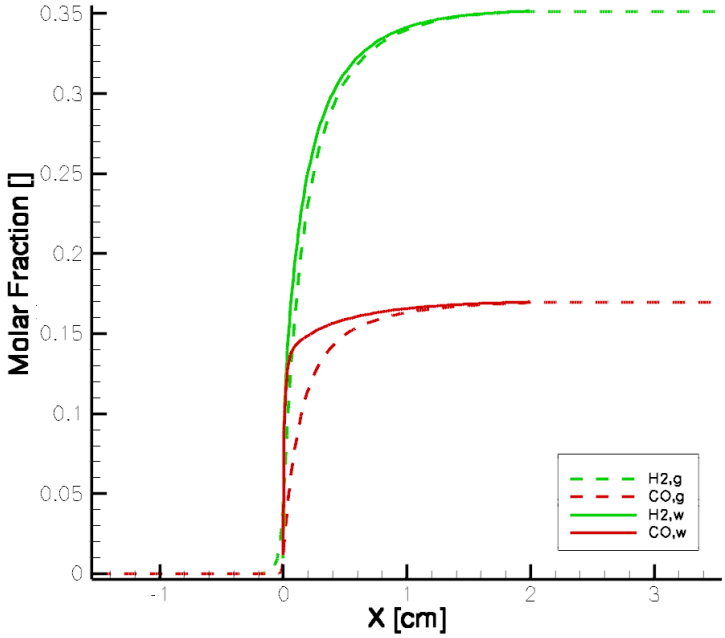

Figure 61: Species profiles of hydrogen and carbon monoxide for both phases

Figure 61 shows at the reactor outlet section (x=3.5cm) a molar ratio of H2CO of about 2 which is consistent with the stoichiometry of the global methane POx reaction. We can also see that during the production of syngas, mainly during the 1st cm, both profiles of each species (boundary layer profile and bulk gas profile) are much closer in the case of hydrogen due to its lower molecular diffusion. This is felt in the model through the external mass transport coefficients.
Finally, the next figure shows the fuel conversion and syngas selectivity along the axial direction of the reactor.

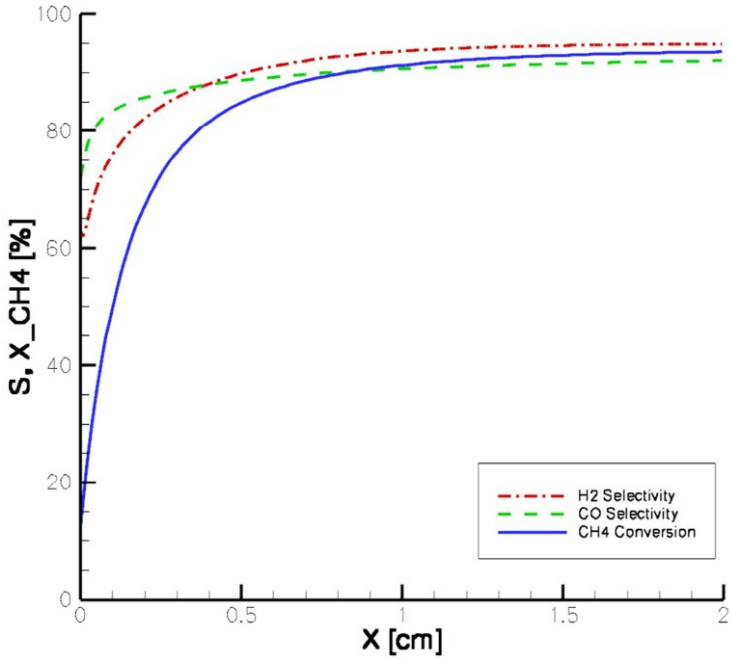

Figure 62: Methane conversion and synthesis gas selectivity

Hydrogen selectivity at the reactor outlet is very high (about 95%) and this is justified by the high carbon to oxygen ratio used in the feed stream ($\lambda=0.27$). As disadvantage a lower fuel conversion is achieved comparing to maximum possible (near to 100%). Starting from this working condition and increasing successively the air to fuel ratio, a higher fuel conversion and a decrease in the syngas selectivity are achieved [1].

6.4 Code application to the FC-District CPOx reactor prototypes

In this section the code previously developed and validated is used to predict experimental data already available for both reformer prototypes built and characterized up to now.

Geometrical characterization of both reactor prototypes as used in the 1D numerical simulations, namely the monolith section, can be seen in the next table.

Table 28: Geometrical properties of the monolith used in both reactor prototypes

Geometrical Properties		
	1st CPOx reactor	**2nd CPOx reactor**
Cell density (cpsi)	400	600
Cell shape	Square	Square
Monolith diameter (cm)	*3.3*	*3.7*
Monolith length (cm)	*4.0*	*3.0*
Porosity (%)	*80*	*70*
Specific surface area (cm^{-1})	*28.00*	*32.27*
Cell hydraulic diameter (cm)	*0.100*	*0.087*
Washcoat thickness (μm)	*20*	*40*

In both CPOx reactor prototypes the suitable boundary conditions, considering the huge importance of molecular and heat diffusion at the catalyst entrance (beginning of the computational domain), should be of another type than those used in the previous section. Hence at the inlet section the *Danckwerts* type of boundary conditions for the gas phase balances was used and *Neumman* type was used for the energy balance of solid phase so that radiation could be considered leaving the reactor boundaries. At the reactor outlet all gradients vanish:

Reactor Inlet	**Reactor Outlet**
$Y_{k,g} - Y_{g,in} + \frac{Y_{k,g} V_{k,g}}{u} = 0$	$\frac{\partial Y_{k,g}}{\partial x} = 0$
$\rho_g C_{p,g} u (T_g - T_{g,in}) - \lambda_g \frac{\partial T_g}{\partial x} = 0$	$\frac{\partial T_g}{\partial x} = 0$
$k_s \frac{\partial T_s}{\partial x} = \sigma \varepsilon_s (T_{g,in}^4 - T_s^4)$	$\frac{\partial T_s}{\partial x} = 0$

As the real composition and loading of the catalyst used in both prototypes remains unknown because these catalysts are commercial and considering that a typical catalyst to be applied in this process belongs to the PGM catalyst group several reaction mechanisms for CPOx of methane over PGM catalysts were tested and it was always chosen the mechanism which better described the already available experimental results for both CPOx prototypes.

6.4.1 1st CPOx reactor prototype

The first prototype was simulated under only 3 working conditions, which are presented in the next table.

Table 29: Working conditions

Simulated working conditions			
	Air Ratio, λ	**VCH4 [NL/min]**	**Tpreheat, mix[°C]**
Case 1	0.29	6	300
Case 2	0.33	6	300
Case 3	*0.33*	*4*	*350*

It was initially assessed which reaction mechanism would describe better the reactor performance against experimental data. A global methane CPOx mechanism from [12] was used.

Results from numerical simulations for these three cases are presented in the next figures. In the same figures data from experimental measurements (exit gas composition) is also shown. Unfortunately, only two experimental gas temperatures were available for this prototype and this sampling was not enough for conclusive comparison purposes.

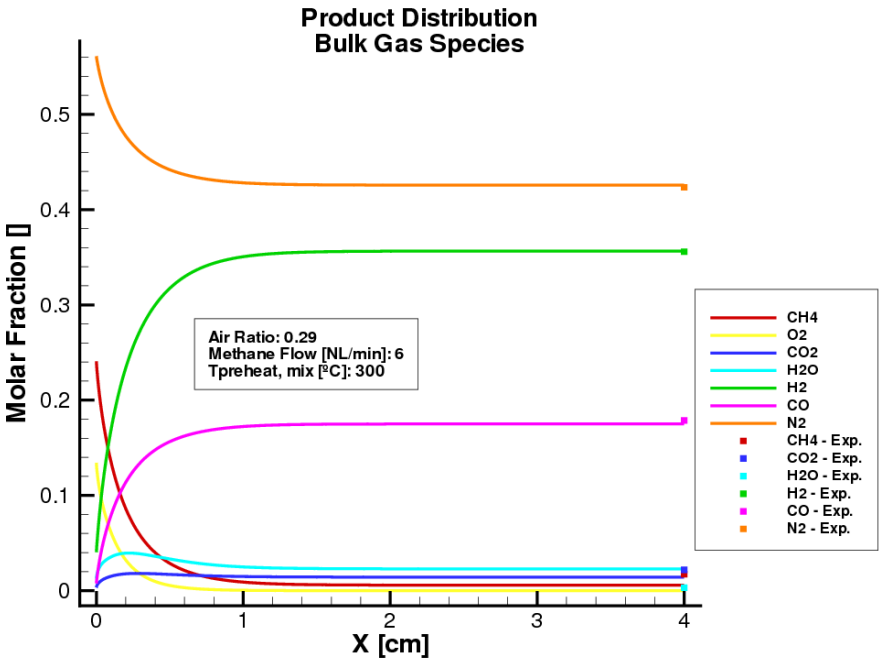

Figure 63: ***Case1*** *- Species profiles from numerical simulations and experimental measurements*

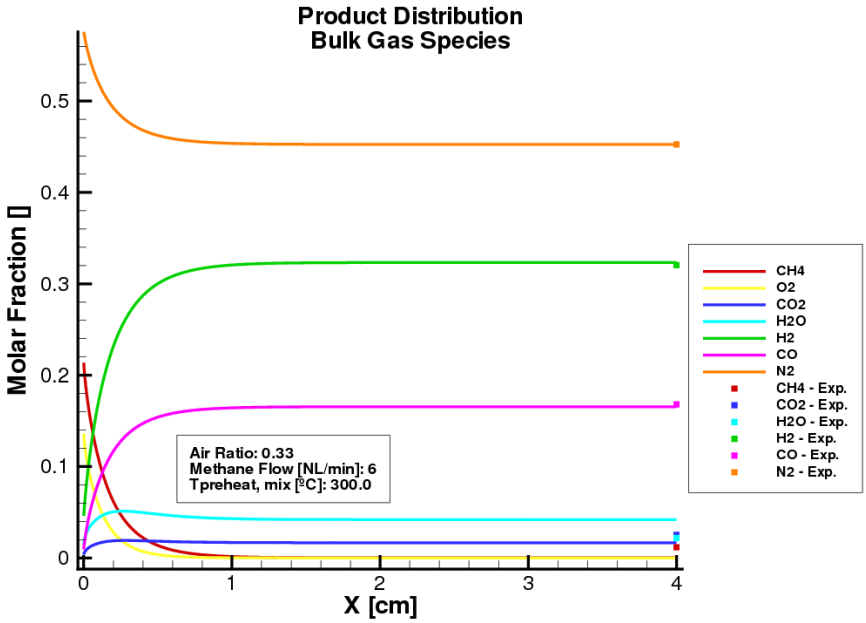

Figure 64: ***Case 2*** *- Species profiles from numerical simulations and experimental measurements*

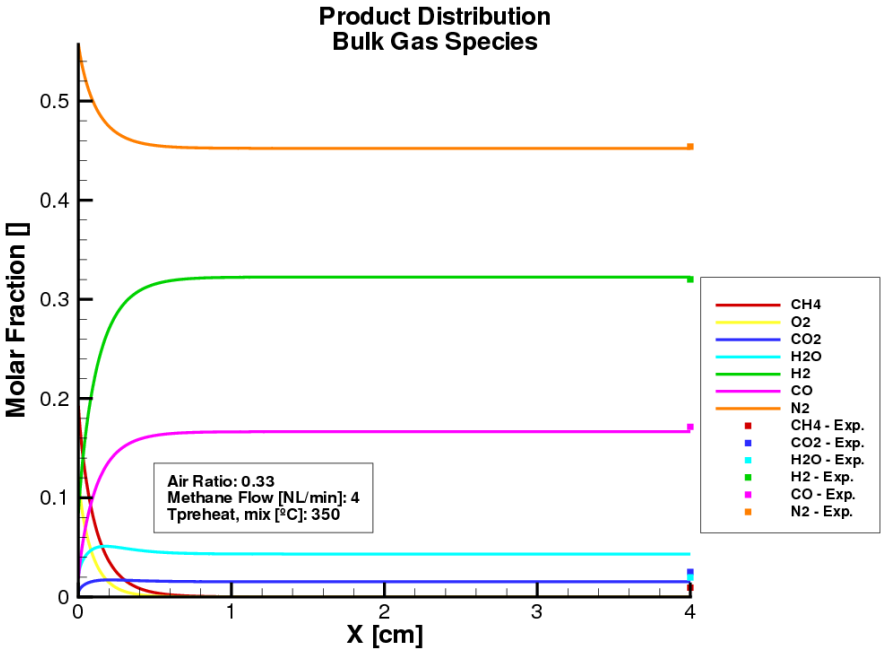

Figure 65: ***Case 3*** *- Species profiles from numerical simulations and experimental measurements*

It can be concluded regarding species profiles that exit gas composition from numerical simulations is in perfect agreement with experimental data, as one can see in the above figures.

6.4.2 2nd CPOx reactor prototype

The next two figures show both thermal and species profiles computed and compared with experimental data. These profiles are just presented here to understand, for a typical CPOx condition and for this reactor geometry, the evolution of the variables considered in the model between the values given by experimental means.

The working condition considered here consists of a **methane volumetric flow rate of 4 NL/min**, an **air ratio of 0.33** and an **inlet temperature of 300ºC**.

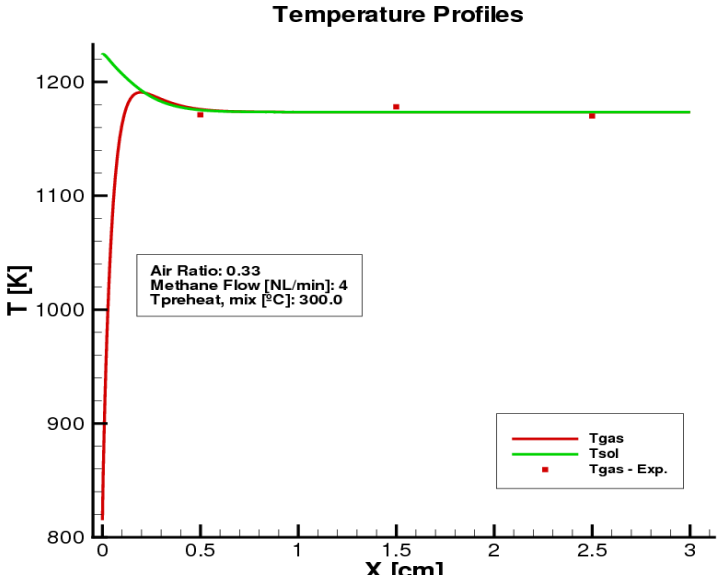

Figure 66: Thermal profiles from numerical simulations and experimental data

Thermal profiles show that the maximum catalyst surface temperature is achieved at the catalyst entrance (for a fresh catalyst) where the incoming feed mixture first reacts via total oxidation of the fuel (according to the indirect CPOx kinetic scheme). After the oxidation of the fuel, highly endothermic reforming reactions are responsible for the decay of the temperature.

The initial high temperatures verified at the catalyst entrance can cause, as the time-on-stream increases, deactivation of the catalyst by sintering or phase transformations in washcoat and catalyst. Following this deactivation mechanism triggered by high temperatures, the catalyst entrance looses activity and the section of higher temperatures inside the monolith, where the CPOx reactions start, moves to downstream.

Once the highest thermal gradients are verified at catalyst entrance we suggested to collect experimental measurements in future reactor prototypes in these regions, namely temperature values.

In Figure 67, the molar profiles of all species of bulk gas flow are shown and for comparison purposes only experimental exit compositions (integral data) are available.
For this working condition and according to the simulated species profiles it is verified in Figure 67 that less than 1 cm of catalyst is enough to ensure a total conversion from reactants to products. However, as expected, when increasing for instance the total flow rate, the length of catalyst needed to achieve equilibrium conditions also increases.

These results, namely the bulk species profiles (Figure 67), were used in 3D numerical simulations to impose a change in the species field and to compute the temperature of the flowing gases by adjusting the enthalpy to the existing species in each section.

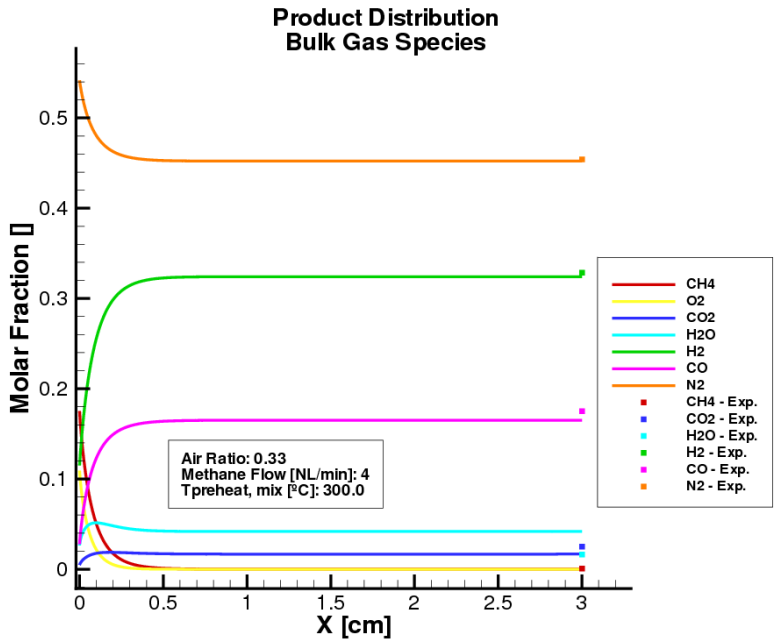

Figure 67: Product distribution and exit experimental data

From now on, instead of the complete thermal and species profiles along the axial direction of the monolith, only a comparison between the values achieved via numerical simulations and those available from experimental tests is presented. Thus, in the following four figures **an air ratio variation [0.29, 0.31 and 0.33] is considered, keeping constant the volumetric methane flow rate of 6NL/min and an inlet temperature of 300ºC**.

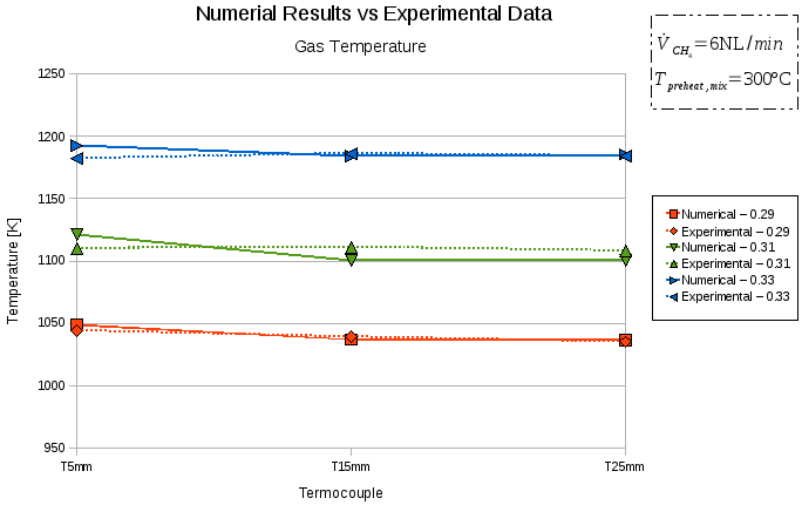

Figure 68: Numerical and experimental gas temperatures varying the air ratio.

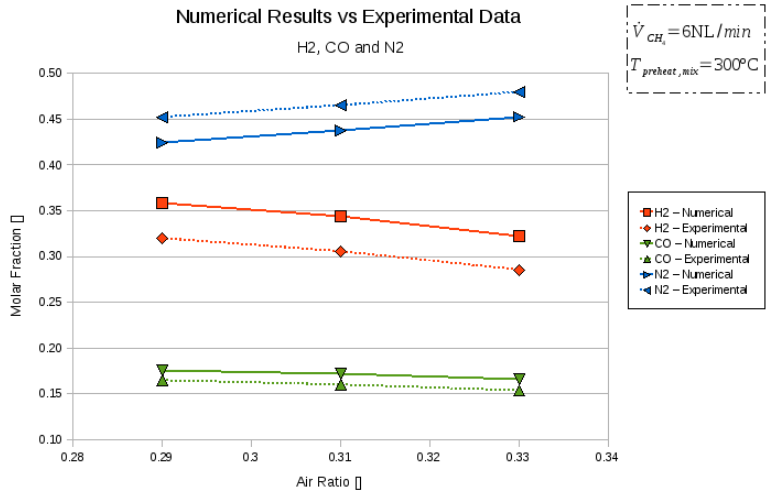

Figure 69: Numerical and experimental molar fractions for hydrogen, carbon monoxide and nitrogen varying the air ratio.

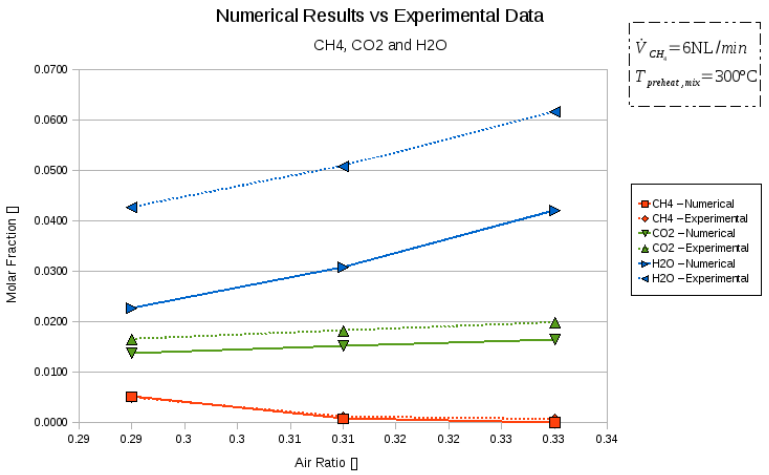

Figure 70: Numerical and experimental molar fractions for methane, carbon dioxide and water

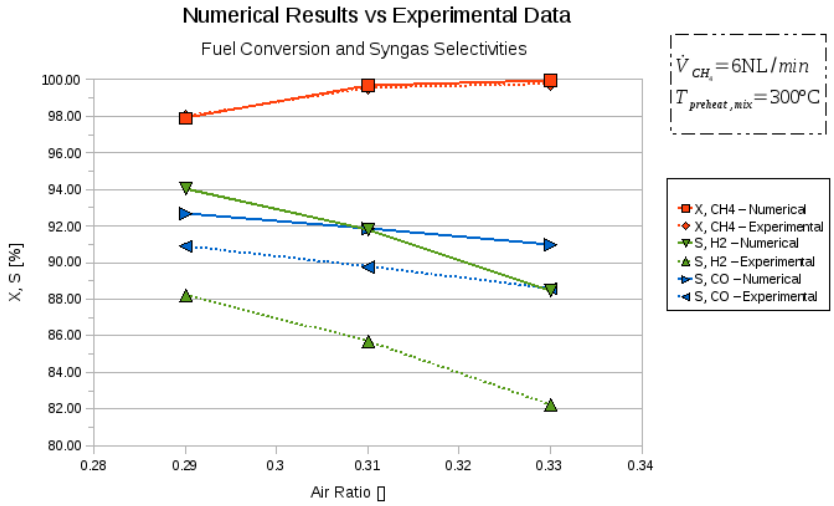

Figure 71: Numerical and experimental methane conversion and synthesis gas selectivity

Gas temperatures obtained via numerical simulations are quite close to measured temperatures. However, there is a slight difference concerning the hydrogen selectivity (Figure 71) since experimental measurements show less hydrogen and more water than the numerical simulations (Figure 69 and Figure 70). Concerning the CO selectivity, the difference between experimental and numerical results is less significant.

The fuel conversion is similar both in numerical simulation results and experimental measurements, as one can see in methane molar fraction at outlet section (Figure 70).

In the next set of graphs **it is kept constant an air ratio of 0.31 and methane volumetric flow rate is varied [2, 4, 6, 7 and 8 NL/min]. An inlet temperature of 300ºC** was considered **for the higher power cases (6, 7 and 8 NL/min)** and **an inlet temperature of 350ºC** was considered **for the remaining flow rates.**

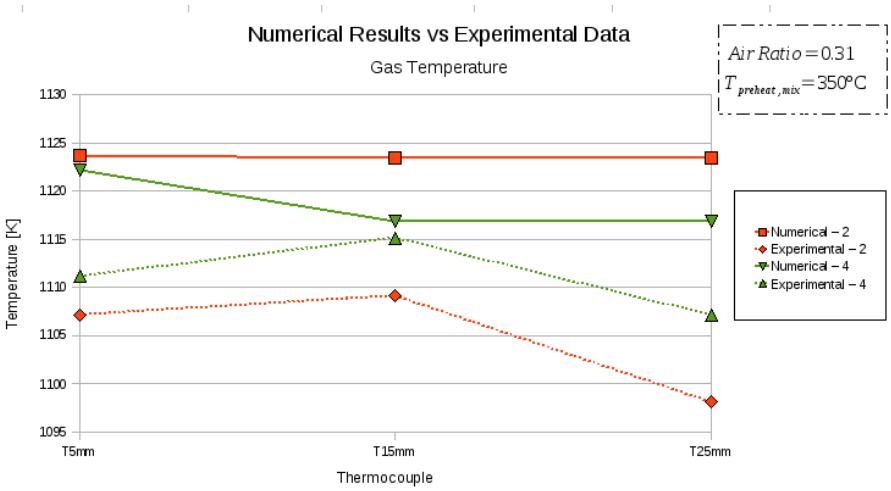

Figure 72: Numerical and experimental gas temperatures for lower power streams

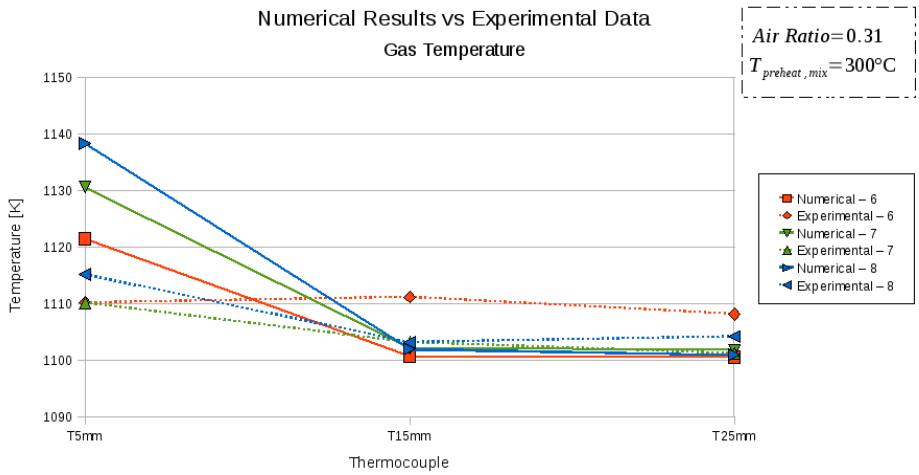

Figure 73: Numerical and experimental gas temperatures for higher power streams

The maximum difference between simulation and experimental gas temperature values happens at the first thermocouple (Figure 73). As methane flow rate decreases the temperature difference between values also decreases in this section.

In all gas temperature values from numerical simulations a tendency is clear for the evolution of temperatures between these three positions:

- - from section x=15mm to x=25mm practically there is no temperature variation for low flow rates, however as the flow rate increases it begins to show a little temperature decrease between these sections. This little temperature gradient is mainly due, as before mentioned, to the need of more catalyst length to achieve equilibrium conditions;
- - from section x=5mm to x=15mm gas temperatures always decrease and the temperature difference increases as the power stream increases.

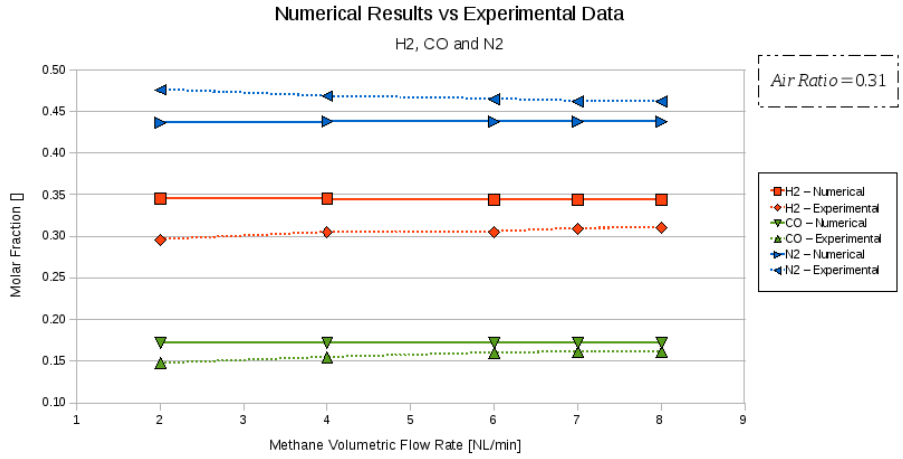

Figure 74: Numerical and experimental reformate compositions: H2, CO and N2 molar profiles

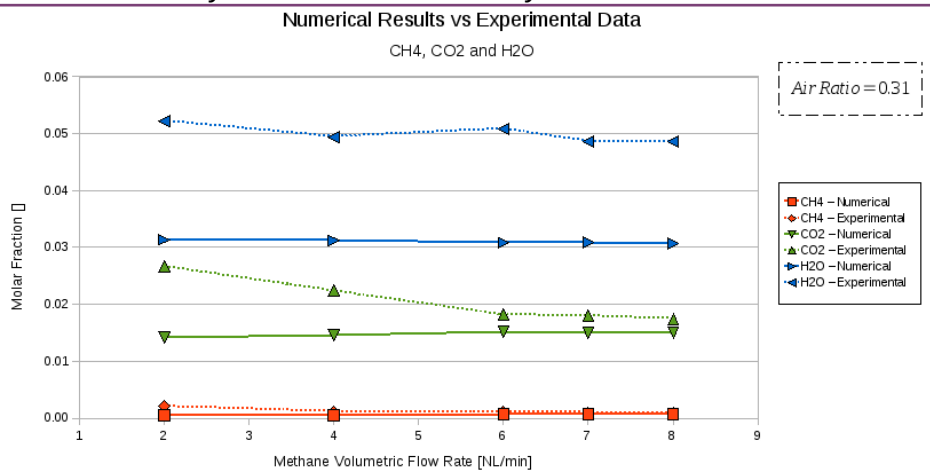

Figure 75: Numerical and experimental reformate compositions: CH4, CO2 and H2O molar profiles

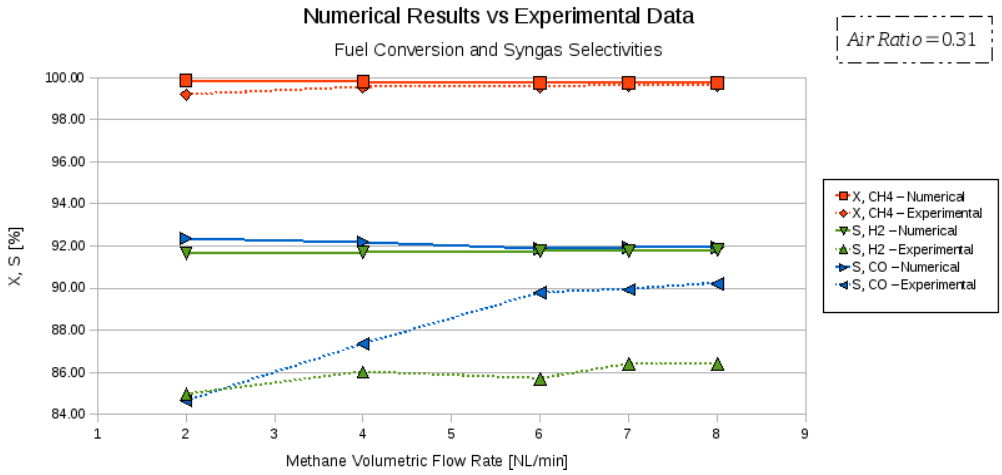

Figure 76: Numerical and experimental methane conversion and synthesis gas selectivity

Regarding the composition of the reformate stream, numerical simulations predict more hydrogen yield (Figure 74) and less water content (Figure 75) than experimental measurements. As a result lower hydrogen selectivity was achieved in experimental measurements comparing to numerical simulations (Figure 76). Concerning the methane conversion both experimental and numerical results are quite close.

Numerical simulations show that varying the fuel flow rate while keeping constant air ratio, causes both solid and gas thermal profiles to vary significantly, namely in the first section (x=5mm) of the monolith. However, reformate exit composition does not vary significantly showing that mass transfer limitation regimes do not differ much in the range of flow rates simulated and that the length of the monolith is more than enough to ensure equilibrium conditions at the catalyst outlet section.

6.5 Conclusions

A complete physical/chemical model for transport and kinetics was implemented for 1D catalytic heterogeneous reactions analysis. The base model is able to work with any detailed chemical reaction mechanism since it is available in CHEMKIN format, but other global reaction mechanisms can be easily incorporated into the code. The numerical implementation has proven to be very robust and its results were validated against reference and experimental data.

The main purpose of the present work was to create a tool designed to assist reformer improvements. Thus, numerical simulations using the tool created were performed, with the same working conditions used in experimental characterization of both CPOx reactor prototypes built up to now in the FC-DISTRIC framework.

For the first reformer prototype, results from numerical simulations have revealed a perfect agreement with experimental data concerning the reformate composition in the simulated working conditions.

Regarding the second CPOx reactor prototype the gas temperatures obtained via numerical simulations are quite close to the experimental measurements and experimental exit gas composition is also in the range of predicted accordingly to the numerical simulations.

7. Conclusions

A complete physical/chemical model for transport and kinetics was implemented for 1D catalytic heterogeneous reactions analysis. The numerical implementation has proven to be very robust and its results were validated against reference and experimental data. Results from numerical simulations have revealed a good agreement with experimental data in the simulated working conditions.

Two prototypes of the CPOx reformer were successfully simulated as well as one heat exchanger and one mixer component.

Predictions were made concerning flow shape, pressure drops, temperatures and other important factors for each component.

The conclusions obtained for the reformer have helped design the next prototypes.
For the mixer and heat exchanger new prototypes haven't been designed.

Regarding further simulation work, simulations of more working points are being prepared in order to have a detailed analysis of all the span of working conditions to which each component will be subjected.

8. Acknowledgements

The FC-DISTRICT Consortium would like to acknowledge the financial support of the European Commission under the Seventh Framework Program.

9. References

[1] J. E. P. Navalho, M. A. A. Mendes, J. M. C. Pereira, J. C. F. Pereira, “Análise em Regime Estacionário da Oxidação Parcial Catalítica de Metano em Ródio”. In Proceedings of “10º Congresso Ibero-Americano em Engenharia Mecânica”, Porto, Portugal, 2011. Faculty of Engineering of University of Porto, p. 887-898.

[2] E. M. Sparrow et. al., “Flow separation in a diverging conical duct: Effect of Reynolds number and divergence angle”

[3] S. Lee, R. Aris, “On the effects of radiative heat transfer in monoliths”, *Chemical Engineering Science*, **32**:827-837, 1977.

[4] R. Schwiedernoch et al., “Experimental and numerical study on transient behaviour of partial oxidation of methane in a catalytic monolith”, *Chemical Engineering Science*, **58**:633-642, 2003.

[5] G. Vesser, J. Frauhammer, “Modelling steady state and ignition during catalytic methane oxidation in a monolith reactor”, *Chemical Engineering Science*, **55**:2271-2286, 2000.

[6] O. Deutschmann, L. Schmidt, “Modelling the partial oxidation of methane in a short-contact-time reactor”, *AIChe Journal*, **44**:2465-2477, 1998.

[7] J. Slaa et al., “Partial oxidation of methane to synthesis gas over Rhα -Al2O3 at high temperatures”, *Catalysis Letters*, **43**:63-70, 1997.

[8] J. Navalho et al., “Modeling CH4 catalytic partial oxidation on Rh coated monoliths”, CPOx_TR05, EMDESK.

[9] A. Donazzi et al., “Catalytic partial oxidation of methane over a 4% Rhα -Al2O3 catalyst. Part I: kinetic study in annular reactor”, *Journal of Catalysis*, **255**:241-258, 2008.

[10] A. Donazzi et al., “Catalytic partial oxidation of methane over a 4% Rhα -Al2O3 catalyst. Part II: Role of CO2 reforming”, *Journal of Catalysis*, **255**:259-268, 2008.

[11] A. Beretta et al., “Experimental and modeling analysis of methane partial oxidation: transient and steady-state behavior on Rh-coated honeycomb monoliths”, *Industrial & Engineering Chemistry Research*, **48**:3825-3836, 2009.

[12] I. Tavazzi, “Development of a molecular kinetic scheme for methane partial oxidation over Rhα -Al2O3 catalyst”, *Journal of Catalysis*, **241**:1-13, 2006.